NON-LINEAR VARIABILITY IN GEOPHYSICS

Scaling and Fractals

edited by

D. SCHERTZER AND S. LOVEJOY

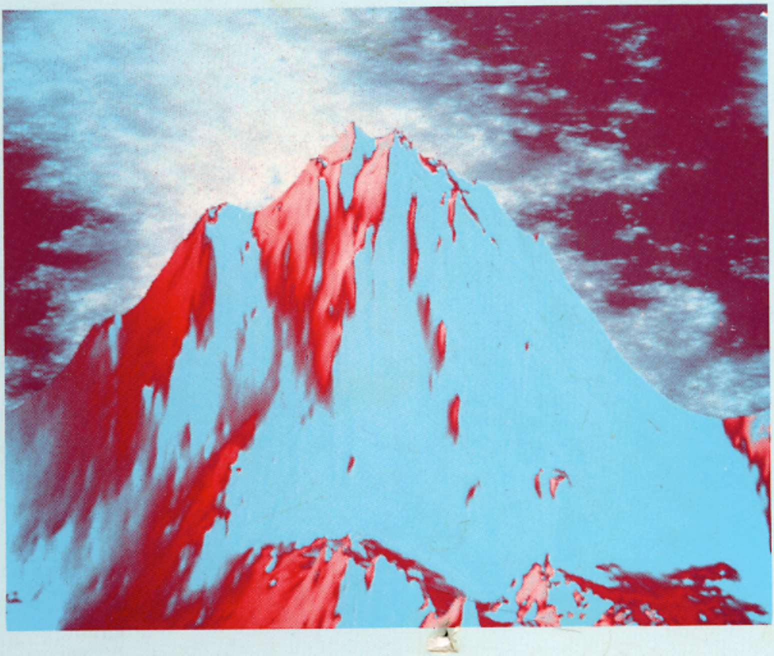

KLUWER ACADEMIC PUBLISHERS

MULTIFRACTAL ANALYSIS TECHNIQUES AND THE RAIN AND CLOUD FIELDS FROM 10^{-3} TO 10^{6}m

Shaun Lovejoy, Daniel Schertzer*
Department of Physics, McGill University,
3600 University st., Montreal, Qué., H3A 2T8,
CANADA

ABSTRACT. We discuss the scaling properties of the rain and cloud fields over the range of ≈1mm to ≈1000km. We find that these fields are multifractal; i.e. the weak and intense regions scale differently, involving multiple fractal dimensions. We re-evaluate several early (mono-dimensional) analyses and argue that failure to account for the multifractal nature of the fields has in several instances lead to spurious breaks in the scaling symmetry. A related result is that area-perimeter exponents no longer yield the dimension of the perimeters, and that the interpretation of the distribution of isolated cloud or rain areas must be modified.

Empirically, we use two recent multifractal analysis techniques: Probability Distribution/Multiple Scaling (PDMS) and Trace Moments to analyse blotting paper traces of rain drop impacts (≈1mm to 128cm), lidar reflectivities from raindrops (≈3m to 540m), and satellite data from both 100m to 100km and 8km to 256km. The conclusions support the idea that the atmosphere has a multifractal structure over this large fraction of the meteorologically significant length scales.

Applications of the results discussed here include resolution independent methods of remote sensing, anisotropic space/time transformations (generalizations of Taylor's hypothesis of frozen turbulence) which we show holds in rain, as well as a method of correcting radar for (mono)fractal effects not included in the standard theory of radar measurements of rain.

1. INTRODUCTION

1.1. The need for systematic study of the scaling properties of atmospheric fields

In spite of its obvious importance for understanding and predicting the atmosphere, no systematic study of scale dependence of atmospheric fields has yet been undertaken. The development of new in situ and remote measurement techniques coupled with rapid advances in computing power now provide the impressive sources of data needed to attempt such a study. What is perhaps most important of all is the equally rapid series of advances in our understanding of non-linear dynamical systems, scaling and (multi)fractals. In particular, multifractal measures are much more relevant in geophysical applications than fractal sets since geophysical quantities are best described as measures, with empirical data being functional approximations[1] to the latter which depend on the resolution of the sensor. Multifractal measures are characterized by their scale-invariant (co)-dimension function which is an exponent function describing the variation of the probability distributions with scale[2]. The geometry of sets and their associated fractal dimensions are secondary; the scale invariant dynamics (characterized by the generator of the measure) play the primary role.

---

*EERM/CRMD, Météorologie Nationale, 2 Ave. Rapp, Paris 75007, FRANCE.

[1] Since the underlying multifractal measures are singular, the measurements (which are typically spatial and/or temporal integrals) do not "approximate" the measurements in a simple way.

[2] Since the codimension is related to the lof of the probability distribution, it is formally analogous to the entropy - see Schertzer and Lovejoy (1990a) for more on this "flux dynamics".

D. Schertzer and S. Lovejoy (eds.), Non-Linear Variability in Geophysics, 111–144.

In this paper we describe two fairly new multifractal analysis methods (the "Probability Distribution/Multiple Scaling" technique and the "Trace Moment" technique), applying these methods to satellite radiance fields, as well as lidar and blotting paper measurements of rain drops overall, spanning the range of scales of ≈1mm to ≈1000km. Finally, in appendices, we re-examine some conventional (mono-dimensional) analysis techniques (such as area-perimeter relations), and show how they can be fit into a multifractal framework.

The need for new data analysis techniques can be appreciated by considering that virtually the only commonly used geophysical data analysis technique that enables one to directly compare the small and large scale statistical properties of fields is Fourier analysis[1]. In spite of its obvious importance, it should be recalled that the resulting energy spectra are only second order statistics[2], and are not particularly robust (i.e. when applied to highly intermittent data, large samples may be needed to obtain good estimates of the ensemble averaged spectra). If the fields were mono-dimensional fractals, then the scaling of the second order moments (characterized by the spectral exponents) would provide nearly complete information about the scaling properties of the field. However, this is generally not the case; multifractal techniques are required to allow for systematic study of the scaling of moments of all orders (or equivalently of weak and strong fluctuations separately), over wide ranges of scale.

In a series of papers - Lovejoy (1981, 1982), Lovejoy and Schertzer (1983, 1985, 1986, 1990a), Lovejoy and Mandelbrot (1985), Schertzer and Lovejoy (1983, 1984, 1985, 1986, 1987a,b, 1988, 1989, 1990, Lovejoy et al. (1987), and Schertzer and Lovejoy (this volume) -, we have argued that we may expect the atmosphere to exhibit scaling, fractal structures. Although we do not wish to repeat these arguments in detail, the basic idea may be simply expressed. If we consider scaling as a symmetry principle (i.e. the system is unchanged under certain scale changing operations), then in the spirit of modern physics, we may tentatively assume (a first approximation), that the symmetry is respected except for symmetry breaking mechanisms.

In the atmosphere, the scaling symmetry is obviously broken at one extreme by the finite size of the earth, and at the other extreme, at scales of ≈1mm, by damping due to viscosity. Atmospheric boundary conditions such as topography (see Lovejoy and Schertzer (1990a) for an analysis) are also multiply scaling are are not expected to introduce a characteristic length to break the symmetry. This leaves a wide range of factor 10^9-10^{10} in scale where scaling symmetries might hold. In this context, it is worth recalling that it has only been in the last few years that the full generality of the scale invariant symmetry principle has been realized. This has enabled us to go far beyond the qualitative (and very restrictive) ideas of fractals as self-similar geometric objects with a single fractal dimension. It can now be quantitatively understood as a system composed of two totally distinct elements unified by the formalism of Generalized Scale Invariance (see Schertzer and Lovejoy (1983, 1985, 1986), and especially in (1987a, b)). The first element is a scale changing operator T_λ which reduces scales by the factor $\lambda \geq 1$; scaling implies $T_{\lambda_1\lambda_2}=T_{\lambda_1}T_{\lambda_2}$ and hence that T_λ has the form $T_\lambda = \lambda^{-G}$ where G the generator of the (semi-group) of scale changing operators (=1 for self-similar, isotropic systems). A power law form of this type ensures that the small and large scales are related only by (dimensionless) scale ratios; hence that over this range, the system has no characteristic size. An immediate consequence is that the operation required to go from one scale to another can be far more complex than simple geometrical magnifications (e.g. self-similarity), hence the rejection of self-similarity does not imply a rejection of scaling. The standard meteorological argument that since the large scale is "apparently" two dimensional due to the stratification caused by gravity, and the small scale is "apparently" three dimensional, is therefore not relevant to the issue of scaling. The second element of a scale invariant system is a multifractal measure that is invariant under the application of T_λ. In turbulence, the basic scale invariant multifractal measure is presumably the energy flux density, since this quantity is exactly conserved by the non-linear terms in the Navier-Stokes equation. In the atmosphere, other scale invariant multifractal measures will be necessary to account for other conserved quantities.

---

[1] Although formally autocorrelation functions contain the same information, they are usually only used to obtain the 1/e point, which when combined with the ad hoc assumption of exponential decorrelations (and hence the absence of scaling), is used to obtain the decorrelation length. When there is scaling the autocorrelations decay algebraically rather than exponentially and the decorrelation length is no longer the 1/e point, but is rather the outer scale of the scaling regime which in geophysics can be many orders of magnitude larger.

[2] They are simply related to the Fourier transform of the autocorrelation function.

GSI allows for so much generality, that not only can the stratification of the atmosphere be easily accounted for in a single scaling regime (intermediate between two and three dimensional turbulence), but also, differential rotation (associated for example with cloud "texture") and even variable Coriolis parameters can be dealt with. It also provides a natural framework for analysing and modelling the space/time strucutre of various fields and hence for investigating the issues of prediction and predictability[1]. We are now faced with the task of restricting our attention to the sub-classes of scaling appropriate to the atmosphere (for example by restricting the class of generators G in some way). Ultimately, such restrictions will have to be derived theoretically from dynamical principles. Unfortunately, the relation between the scale invariant symmetry and the non-linear atmospheric dynamics is far more difficult to discern than in other areas of physics (particularly quantum mechanics) where due to the linearity of the equations, the dynamics and symmetries are synonymous. We therefore give special attention to the empirical characterization of both scaling and symmetry breaking.

1.2. Developing Resolution-independent measurement techniques

Below, we restrict our attention to studies of the rain and associated cloud fields. From our perspective - aside from their intrinsic interest - the rain reflectivity, cloud radiance and lidar[2] reflectivity fields have the advantage of being among the best measured meteorological fields: radar, satellites and lidar all provide excellent remotely sensed data spanning wide ranges of time and space scales. High quality in situ and aircraft data are also available. Naturally, a full statistical description of either field requires knowledge of properties of the measures defined by the drop volumes (V_i) and their distribution in space ($\underline{r}_i$), whereas the above techniques do not measure these quantities directly. Some reasonably direct information is available from both the lidar and blotting paper methods discussed in sections 3,4; however, for investigating the large scales (≈1-10^3km) we rely on the indirect information supplied by radar and satellite data. For example, the radar measures the ("effective") reflectivity[3] (Z_e) of the (n) drops in the (microwave) pulse volume:

$$Z_e \propto \left| \sum_i^n V_i e^{i\underline{k}\cdot\underline{r}_i} \right|^2 \tag{1.1}$$

(where $\underline{k}$ is the radar wave vector), whereas, the (volume averaged) rainrate (R) is a different measure:

$$R \propto \sum_i^n w_i V_i \tag{1.2}$$

where w_i is vertical velocity of the i^{th} drop. At visible and infra red wavelengths, the relationship between the rain/cloud measures and the reflected/emitted radiation fields is even more indirect[4], however such measurements still give us valuable information about the scaling symmetries of the rain field. For example, symmetry breaking in the latter will be evident in the former. More generally, the multiple scaling of these fields implies that the values of sensor averages depend critically on the sensor resolution, hence for example, if remotely sensed data are to be used for estimating rain or cloud amounts, then the resolution dependencies of both the in situ (ground truth) data, and remotely sensed data must be systematically removed (e.g. by using the associated scale invariant codimension functions). Such a

---

[1] In geophysical flows, each distance scale has a corresponding time scale, hence scaling is expected in space-time. Section 4 gives empirical evidence in rain showing that time is "stratified" with respect to the horizontal space coordinate i.e. space-time transformation should be anisotropic, and appendix E gives a theoretical discussion.

[2] A lidar is the laser analogue of a radar.

[3] Normally, the cumbersome adjective "effective" is dropped and and the symbol Z is used rather than the more correct Z_e. See section 3. for more details.

[4] See Davis et al. (this volume) for more discussion of this radiative transfer problem.

resolution-independent approach to remote sensing will require both careful measurements of the statistical properties of the fields over wide ranges in scale, combined with stochastic modelling of the fields themselves (see e.g. Wilson et al this volume).

2. MULTIFRACTAL MEASURES, CODIMENSION FUNCTIONS AND THE PROBABILITY DISTRIBUTION / MULTIPLE SCALING (PDMS) TECHNIQUE

2.1. Discussion

Based on studies of certain fractal sets obtained either as purely geometric constructs, or associated with certain stochastic processes, Mandelbrot [1982] used these sets as models of the geometry of various natural systems. However, few natural systems are sets (they are usually best treated as fields or measures), and it soon became clear - Hentschel and Proccacia (1983); Grassberger (1983); Schertzer and Lovejoy (1983); Benzi et al. (1984), Frisch and Parisi (1985) - that such measures are fundamentally characterized not by a single dimension, but by a dimension function (sometimes called the "spectrum of singularities"). Furthermore, this dimension function is simply related to the probability distribution. In fractal sets, the concept of fractal dimension is important because it is invariant under transformations of scale. In fractal measures, the notions of scaling (or scale invariance) and the generator of the measure are more basic.

Geophysical systems typically have variability extending from a large "external" scale L down to very small scales η (often 1 mm or less) and are therefore usually observed (literally "measured") at scales (l) with scale ratio $l/\eta>>1$. It is therefore natural to consider the underlying phenomenon as a fractal measure, and the empirically accessible measurements (e.g., satellite photos) as a series of associated functions (denoted $f_\lambda(\mathbf{r})$), whose properties will depend greatly on the averaging scale ratio $\lambda = L/l$ (e.g. l is the size of a pixel). Using the external scale to define scale ratios in this way, we find that qualitatively, the relationship of a series of higher and higher resolution images (i.e. f_λ as $\lambda\rightarrow\infty$) to the underlying multifractal measure is that as the resolution increases, the structures are increasingly sharply defined, are found to occupy a decreasing fraction of the image, while simultaneously increasing in value (e.g., brightening) to compensate. Since over our range of interest, there is no characteristic scale, this behaviour is algebraic and can be expressed as follows (algebraic relations are for the moment valid to within proportionality constants and log corrections; see below)

$$\Pr(f_\lambda > \lambda^\gamma) \approx \lambda^{-c(\gamma)} \tag{2.1}$$

where Pr means probability, γ is the order of singularity associated with the (nondimensionalized, see below) pixel value f_λ, and $c(\gamma)$ is the associated codimension (the dimension of the underlying space (d) minus the corresponding dimension $d(\gamma)$). Equation (2.1) is the general characterization of multifractal fields and is the generic result of multiplicative cascade processes (Schertzer and Lovejoy (1987a,b)). This equation shows that $c(\gamma)$ is directly related to the probability distribution. This fact will be used below as the basis for empirically estimating $c(\gamma)$. Qualitatively, γ is the resolution-independent characterization of the intensity of the feature with brightness f_λ, whereas, $c(\gamma)$ is the resolution independent characterization of the image fraction occupied by features with brightness f_λ.

For those who are familiar with multifractals, it is worth noting here that we have denoted the orders of singularities by the symbol γ because the atmospheric quantities of interest are modelled by densities of multifractal measures (such as f) and γ gives the orders of these singularities directly. In other systems such as phase space portraits of strange attractors (e.g., Halsey et al. (1986)), it is more usual to treat the singularities of the measures (rather than their densities) usually denoted by the symbol α; the relation between α and γ being $\gamma=d-\alpha$ where d is the dimension of space in which the process occurs. Furthermore, we use the codimension function $c(\gamma)$ rather than a dimension function since we are really interested in a family of measures each identical except for the dimension of the space in which it is embedded (in some applications it is even useful to take the latter as a fractal set, e.g. the global meterological measuring network), and the codimensions specify the probabilities independently of the latter. In contrast, in studying strange attractors, d is usually kept fixed and the dimension is denoted usually $f(\alpha)$. We therefore have[1] $f(\alpha)=d-c(d-\alpha)$.

We can now appreciate some of the difficulties encountered in many of the early studies, where multifractal phenomena were analyzed with methods originally designed for studying sets (e.g., area-perimeter relations, distribution of areas, dimensions of graphs, box counting: see appendices A and B). Even before the analysis begins, experimental measuring devices integrate the underlying measure scale ratio λ, converting it into a (spatially or temporally discretized) function. This function is then converted into a set with the same resolution, typically with the help of thresholds. Finally the geometric properties of the resulting set are characterized by (at most) a few exponents (e.g., dimensions, area-perimeter exponents) essentially by degrading the resolution of these sets. Although careful and systematic study of the properties of the sets as functions of scale and threshold (such as with "functional box counting" - Lovejoy et al., 1987; Gabriel et al., 1988) can be used to estimate $c(\gamma)$, such methods are indirect and are less satisfactory than other methods such as trace moments (Schertzer and Lovejoy, 1987a) or the PDMS method (Lavallée et al., this volume). For comparison, functional box-counting exploits (2.1) by transforming the function f_λ into an exceedance set (see Appendices A, B) and covering the latter with larger and larger boxes. The fraction of the scene covered by boxes of scale λ is the probability in (2.1). The method works by degrading the resolution of the exceedance sets, rather than of the measures themselves. The approach described below is more straightforward and statistically robust, since it is defined directly by the measures f_λ rather than via associated sets. In contrast, the use of what might be termed "monofractal" analysis techniques (i.e., techniques designed primarily for analyzing sets) can easily lead to seemingly contradictory results, and even to spurious breaks in the scaling (see appendices).

2.2. The Probability Distribution Multiple Scaling (PDMS) technique

We seek to directly apply (2.1) to determining the scale invariant codimension function $c(\gamma)$. We have already introduced the dimensionless scale ratio λ to nondimensionalize the scales, we must now discuss how to nondimensionalize f. This is conveniently done by using the large-scale average f_1, as a reference value for the measure since $\lambda=1$ implies l=L, the external scale of the image[2]. Using an overbar to denote the values of the function normalized in this way, we write: $\bar{f}_\lambda = f_\lambda/f_1$ Theoretically, the latter should really be the ensemble (i.e., climatological) average of the random process at scale ratio $\lambda=1$; the sample average being an approximation to the latter[3]. We therefore obtain

$$\Pr\left(\bar{f}_\lambda > \lambda^\gamma \right) = F\lambda^{-c(\gamma)} \quad (\lambda\geq 1) \tag{2.2}$$

where F is a prefactor which is only a function of γ and $\log\lambda$ (for example, if F contains a $(\log\lambda)^\Delta$ dependency, Δ is called a "sub-codimenison"). Taking logs and rearranging, we obtain

$$c(\gamma) = -\frac{\log \Pr\left((\log \bar{f}_\lambda)/(\log\lambda) > \gamma\right)}{\log\lambda} - \frac{\log F}{\log\lambda} \tag{2.3}$$

Hence, plotting the normalized log probability distribution ($-\log\Pr/\log\lambda$) against the normalized log intensity ($\log\bar{f}_\lambda/\log\lambda$) we obtain the resolution (λ) independent function $c(\gamma)$. To empirically test this multiple scaling behavior, we therefore take our empirical field and successively degrade it by averaging, obtaining a series of functions $f_{\lambda_1}(\mathbf{r})$, $f_{\lambda_2}(\mathbf{r})$, $f_{\lambda_n}(\mathbf{r})$, which with decreasing λ simulates the results of sensors with successively lower resolutions with $L_l/\eta>\lambda_s\geq\lambda_n>1$, with λ_s the ratio of external scale to the sensor scale (if we define L as the external scale of the image, then this is the largest ratio accessible from

---

[1] Do not confuse this function f or the value α (which we cite here purely for reference) with the quite different f, α used in this paper.

[2] In Lovejoy and Schertzer (1990c), a slightly different normalization was used.

[3] In two dimensions, $\bar{f}_1 = \frac{1}{L^2}<\int_L\int_L f d\mathbf{x}>$ where "< >" indicates ensemble averaging, L is the entire image size.

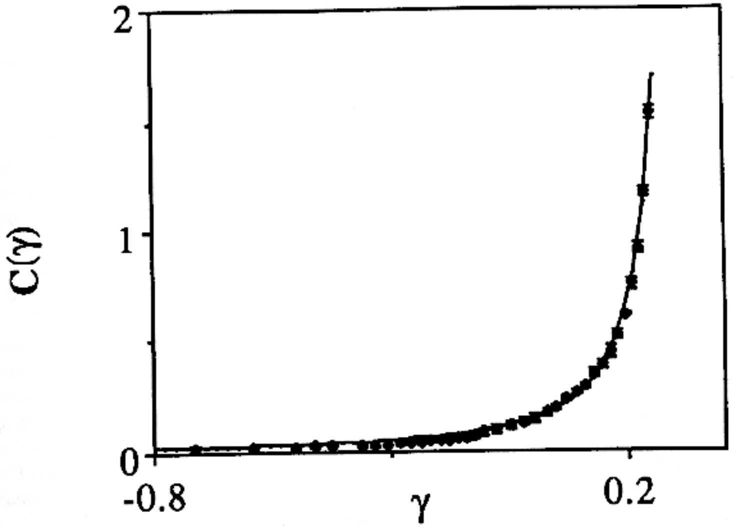

Fig. 1a: PDMS estimates of the function c(γ) from the five visible GOES images over 1024X1024 km at 8km resolution discussed in the text. The points indicate the mean c(γ) curve obtained by averaging the 6 individual c(γ) functions obtained at 8, 16, 32, 64, 128, 256 km scales (the histograms associated with 512, 1024 km did not have enough points, and were not used). The error bars indicate one standard deviation (and were of average magnitude ±0.011) showing that the c(γ) function was nearly scale invariant over this range. The solid line is the least mean squares fit to the universal form (eq. 2.4) ($\alpha'= -1.70$, $\alpha=0.63$). The standard error of the fit was ±0.011.

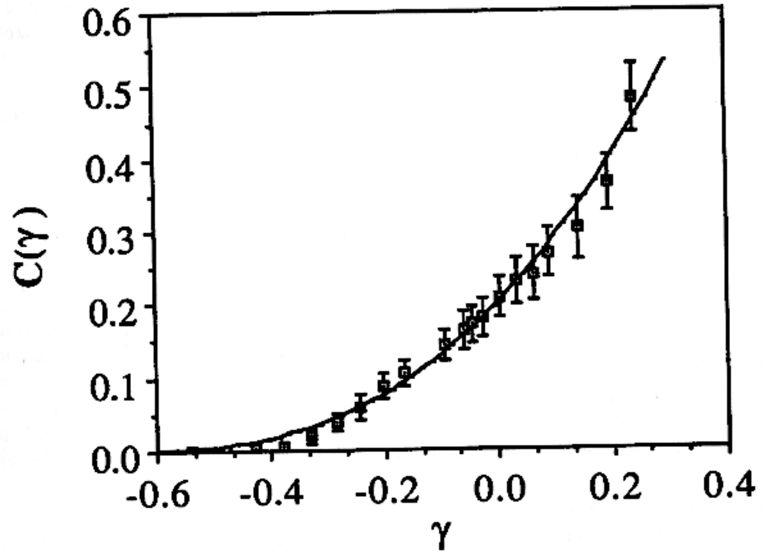

Fig. 1b: PDMS estimates of the function c(γ) from the five infra red GOES images discussed in the text with the same range of scales and format as fig. 2.1a. The mean standard error was ±0.023, and the best fit regression to eq. 2.4 yielded $\alpha'=-2.52$, $\alpha=1.66$. The standard error of the fit was ±0.015.

the data set). Successive factors of 2 can be easily implemented recursively[1]. Note that we must not nonlinearly transform our radiance field (e.g., by transforming from radiances to equivalent blackbody temperatures), since this does not simulate the result of a lower resolution sensor. Furthermore, the normalization based on f at scale ratio $\lambda=1$ implicitly assumes that the probability distribution in (2.2) is either from a single scene or from several independent scenes. If single scenes are used, then we cannot obtain information on the codimension for values of $c>d(A)$, since the corresponding structures would have negative dimensions. However, when many realizations are available, the effective dimension of the sample can be larger, and higher values of $c(\gamma)$ can be determined; see Lavallée et al. (this volume) for discussion of this "sampling dimension." Finally, if many dependent samples are used as in the use of time series of images in A. Seed et al. (manuscript in preparation, 1990), then an "effective" external scale L can be determined from regression (as can f_1).

The Probability Distribution/Multiple Scaling (PDMS) technique refers to the direct exploitation of (2.2, 2.3) to obtain c(γ). This direct method has a number of advantages when compared to the conventional route (via the moments K(h) followed by Legendre transformation; see for example Halsey et al. (1986)) not the least of which is that it avoids the problem of estimating high order moments which may in fact diverge. The PDMS method can be implemented in various ways. In Lavallée et al. (this volume), histograms of all the values of $f_\lambda/\bar{f}_1$ at the various resolutions λ were produced, taking for the value of $\bar{f}_1$ the mean of all the sample spatial averages at scale $\lambda=1$ (the number of "scenes" / satellite pictures, etc.). From the histogram, the largest to smallest values were summed to yield the probability distribution. Finally, c(γ) was determined as the absolute slope of plots of log Pr against log λ for given values of γ. This method has the advantage of readily taking into account the slowly varying prefactor F, since Log F is simply the intercept at $\log \lambda=0$. See Lavallée et al. (this volume) for a much more complete discussion of this method including theoretical considerations and numerical simulations.

In this paper, we used a slightly different method inspired by "functional box-counting" (Lovejoy et al. (1987)), in which the probability distributions at various scales λ was determined differently. The data at highest resolution (λ_s) was covered with a series of lower resolution grids (the "boxes") as explained above. However, rather than using the average value over each box (and create histograms of these averages), we used the maximum value in each box scale λ (denoted $\max_\lambda(f_{\lambda_s})$). Since the function was not averaged, the singularity corresponding to each maximum value was simply estimated as $\gamma=\log(\max_\lambda(f_{\lambda_s}))/\log\lambda_s$. The corresponding c(γ) for each resolution λ was then estimated as $-\log\Pr/\log\lambda$ (we assumed $\log\lambda>>\log F$, ignoring the prefactor in (2.2)). Finally, we took the average c(γ) function over a series of resolutions λ, indicating the scatter with one standard deviation error bars.

Figures 1*a*, 1*b* show the results when this technique is applied to five visible and five infrared GOES[2] pictures over Montreal, respectively. The original (raw) satellite pictures were first resampled on a regular 8 x 8 km grid over a region of 1024 x 1024 km. As can be seen, all the distributions are nearly coincident, in accord with the multifractal nature of the fields. To judge the closeness of the fits, we calculated the mean $c(\gamma)$ curves as well as the standard deviations for 8, 16, 32, 64, 128, and 256 km, finding that the variation is small, being typically about ±0.02 in (γ), which is more accurate than estimates obtained using functional box counting on similar data (Gabriel et al. (1988) found accuracies of about ±0.05).

2.3. Universality classes of c(γ)

We have already argued that the resolution independent codimension function c(γ) is of considerably more interest than particular values of the function. Continuous cascade models, allow us to go even further (Schertzer and Lovejoy 1987a,b, this volume) since it can be shown that c(γ) falls into the the following universality classes (e.g. functional forms):

---

[1] Note that we must not non-linearly transform our radiance field (e.g. by transforming from radiances to equivalent black body temperatures), since this does not simulate the result of a lower resolution sensor. Typically $\lambda_s>>1$ since the sensor resolution is of the order of meters or more whereas the fields typically vary over distances of the order of millimeters.

[2] Geostationary Operational Environment Satellite.

$$c(\gamma) = c_0\left(1 - \frac{\gamma}{\gamma_0}\right)^{\alpha'} \qquad (2.4)$$

where α' and c_0 and γ_0 are the fundamental parameters describing the process characterizing respectively the generator of the cascade, the intermittency, and smoothness of the process. The generator is characterized by the Lévy index α with $1/\alpha + 1/\alpha' = 1$ with the value $\alpha' = \alpha = 2$ corresponding to the Gaussian case, $1<\alpha<2$ with $\alpha'>2$, and $0<\alpha<1$ with $\alpha'<0$. Equation 2.4 can be regarded as a kind of "central limit" theorem for multiplicative processes. When the quantity of interest is conserved by the cascade[1] the cascade generators are normalized and only two parameters are required to characterize the universality class:

$$c(\gamma) = C_1\left(\frac{\gamma}{C_1\alpha'} + \frac{1}{\alpha}\right)^{\alpha'} \qquad (2.5)$$

The value of the parameter α is of particular interest since it is associated with qualitatively different types of cascades[2]. For example, when $\alpha<2$, the generator of the process takes on values near 0 so frequently that all the negative moments diverge (a consequence of "extremal " Lévy generators - see Schertzer et al., 1988; Schertzer and Lovejoy, 1990b, this volume). This yields processes which often have large holes (regions with extremely low values), and may be good candidates for generators in cloud and rain models.

The difficulty in testing these ideas empirically is that the key parameter α' characterizes the concavity of $c(\gamma)$ which is only pronounced when γ and $c(\gamma)$ vary over a substantial range. From the point of view of non-linear regression, to fit c_0, γ_0, α' to the data we find that γ_0 and α' are highly correlated and hence parameter estimates are not very sharp. In Gabriel et al. (1988), functional box-counting was used yielding less accurate estimates of $c(\gamma)$ than those obtained here. The issue was side-stepped by assuming $\alpha'=2$ and testing the consistency of the data with that hypothesis.

Here we improve on these results by determining α' by a least squares regression on the mean of the 8 to 256km curves in fig. 2.1a,b. Maximum likelyhood estimates for the parameter α were found to be: $\alpha=0.63\pm0.035$ and $\alpha=1.66\pm0.37$ for the visible and infra red data respectively[3]. Fig. 2.2a shows the best fit and mean visible and infra red curves. The standard errors in the fit are ±0.011 and ±0.015 respectively. In Lovejoy and Schertzer 1990c, an efficient graphical method of estimating the parameters is outlined which exploits the special properties of the universal $c(\gamma)$ function eq. 2.5: $c(C_1)=C1$, $c'(C_1)=1$ which can be easily verified by inspection. This means that for these (conserved) codimension functions have the property that straight lines with slope 1 passing through the origin will be exactly tangent to $c(\gamma)$ at the value $\gamma=C_1$ independently of the value α. Once C_1 has been determined in this way, α can be determined by specifying one other value of the curve ($c(0)$ usually works well) and solving an algebraic equation for α. For the (non-conserved) quantities analysed below an additional parameter specifies a left/right shift, but the idea is the same. See Lovejoy and Schertzer (1990c) for more details.

The α parameters estimated at these two wavelengths are significantly different since they correspond to α', $\gamma_0<0$ and $\alpha'>2$, $\gamma_0>0$ respectively; it is therefore of some interest to corroborate these findings. The simplest (qualitative) method of distinguishing these two cases, is to consider the graph of $\ln c(\gamma)$. Taking derivates, we find:

$$\frac{d^2 \ln c(\gamma)}{d\gamma^2} = \frac{-\alpha'}{\gamma_0^2}\,\frac{1}{(\gamma/\gamma_0+1)^2} \qquad (2.6)$$

---

[1] For example the energy flux to smaller scales in the dynamical turbulent cascade, or the concentration variance flux in passive scale cascades.

[2] C_1 is the co-dimension of the "support" of the measure corresponding to the unique dimension introduced by Mandelbrot (1974).

[3] The large difference in the maximum likelyhood errors cited here is due at least in part to the fact that we directly estimate α' and $\Delta\alpha = (1+\alpha)^2\Delta\alpha'$ hence this effect alone accounts for a factor 2.7 in difference.

hence for $\alpha'\geq2$ ($1<\alpha\leq2$), $\ln c(\gamma)$ is everwhere convex, whereas, for $\alpha'<0$ ($0<\alpha<1$), it is everywhere concave. This sharp contrast is readily confirmed in fig. 2.2b. These analyses are important not only because they confirm cascade theories, but also because they will help calibrate stochastic rain and cloud models.

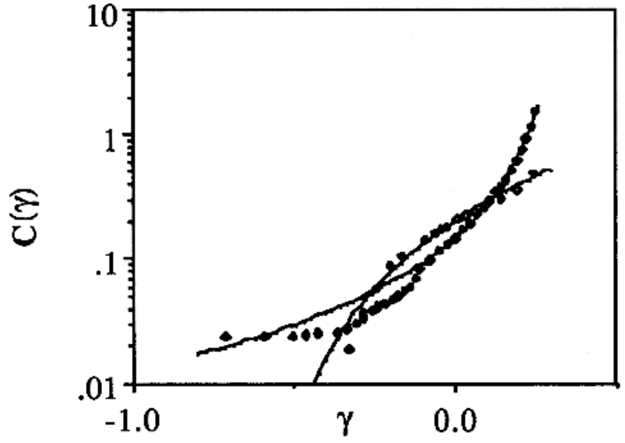

Fig. 2. The same as fig. 1a,b except that the c(γ) axis is in log coordinates. Note that in accord with the best fit values of α (the lines), the visible curve is concave, while the infra red curve is convex.

3. MULTIFRACTAL RAIN MEASURES AND RADAR REFLECTIVITIES

3.1. Multifractal Marshall-Palmer experiment

In the previous sections, we ignored the particulate nature of rain, investigating the properties of the radiance fields without attempting to interpret the latter in terms of the rain (or cloud) measures themselves (i.e. $(V_i, \underline{r}_i)$. In this section, we attempt to obtain $(V_i, \underline{r}_i)$ directly, enabling the statistical properties of Z, R and (in principle) all the radiative transfer characteristics to be determined. The method used is a modern day version of the famous Marshall-Palmer (1948) experiment which was the first to measure the size distribution of rain drops. This experiment – which in the form of a semi-empirical Z-R relation, still provides the quantitative basis of most radar meteorology – consists in using chemically treated blotting paper (that changes from pink to blue when wetted) to record the impacts of rain drops. The drop volume (V) can be fairly accurately estimated from the radius ρ of the coloured stains on the blotting paper. By dropping carefully calibrated drops down the four floors of the stairwell of the Macdonald physics building at McGill University, Marshall and Palmer showed that $V\propto\rho^2$ (with little statistical scatter) which is the relation expected if the penetration depth of the water into the blotting paper is constant. We then show how these results can be exploited to obtain corrections to radar measurements of rain.

Our modern rerun was performed with the help of B. Miville and T, Pham; two third year honours physics students, as part of their honours physics laboratory project. They reran the calibration procedure using the same stairwell as Marshall and Palmer, (finding the same exponent in the V-ρ relation). The improvements were a) the use of much larger (128X128 cm) squares of blotting paper (rather than the 16X24cm size used in the original experiment), b) the digitisation of the results, c) unlike Marshall and Palmer who were interested only in drop sizes (and assumed that the latter were distributed uniformly in three dimensional space, and hence uniformly over the blotting paper), we also recorded the <u>position</u> ($\underline{r}_i$) of the drops (for some more information on the experimental set-up, see Lovejoy and Schertzer (1990b)). By exposing the blotting paper for very short times (≈1s), we attempted to obtain a horizontal intersection of the $(V_i, \underline{r}_i)$ measure. If the latter were isotropic, then knowledge of the statistics of intersections would yield statistical information on the full multifractal $(V_i, \underline{r}_i)$ measure for all subsets with dimension ≥1 (this codimension is the "dimensional resolution" of the blotting paper – see Lovejoy et al. (1986a,b) for a discussion). However, the anisotropy requires us to be more prudent; for example, we must use the elliptical dimension of rain (=2.22±0.07 rather than 3) estimated in Lovejoy et al. 1987 in order to extrapolate to the properties of $(V_i, \underline{r}_i)$ in space (see section 3.2).

In order to sample the horizontal intersection of the rain field, the blotting paper must be exposed for as short a time as possible. In this case, an exposure of ≈1s was obtained, although this is not as short as might be hoped given that rain drop fall speeds are typically 2-5m/s. To put the problem in context, consider very long exposures. In this case, (taking the rain as an (x,y,z,t) process), the blotting paper will record the projection of the rain on the x-y plane. However, the properties of projections and intersections are quite different. Here, the projection relation indicates that any component of the multifractal rain measure with dimension $D \geq 2$ will lead to planar projections (i.e. the projection has dimension 2, and the blotting paper gets wet everywhere), whereas the intersection will have $D_{\cap}<2$ as long as $D<d_{el}$ (where d_{el} is the elliptical dimension of the (x,y,z,t) process).

Fig. 3.1 shows the points corresponding to the centres of the circular blobs on the blotting paper; in this case there are 452 of them. These were digitised along with their radius (to an accuracy of 0.5mm). 452 is a relatively small number of drops with which to estimate dimensions (see the paper by Essex in this volume), however, since $D \leq 2$, it is sufficient. We also analysed two other rain events (with 1293, 339 drops respectively), but these we analysed by hand and are discussed later on. The statistically most sensitive analysis method is to estimate the correlation dimension (as was done in Lovejoy et al. (1986a) for the meteorological measuring network). This is done by considering the function $\langle n(l)\rangle$ which is the average number of other drops in a radius l around each drop. Since there are 452X451/2=101,926 drop pairs, this function contains a great deal of information about the drop clustering. We then define the correlation dimension D_2 as $\langle n(l)\rangle \propto l^{D_2}$. Fig. 3.2 shows that over the range 2mm ≤ l ≤ 40cm, that $D_2 \approx 1.83$ (the subscript refers to the fact that the drops are embedded in a two dimensional space). The large l behaviour deviates below the line because many of these large circles go outside the blotting paper and are therefore biased downwards. At the small scale end, we also obtain a bias due to the finite number of points; for example, clearly $\langle n(l)\rangle \geq 452^{-1}$. We therefore take this as evidence that rainfall is scaling over this range.

In order to extrapolate the $\langle n(l)\rangle$ result from the measured (horizontal) intersection to the full x,y,z space, the strong horizontal stratification of the rain process due to gravity must taken into account. Introducing the codimensions with respect to two and three dimensional embedding spaces $C_3=3-D_3$, $C_2=2-D_2$ (≈0.17 here) and using the formalism of "generalized scale invariance" (Schertzer and Lovejoy, 1985a,b; 1987a,b), in x,y,z space, we expect $\langle n(l)\rangle \propto l^{D_3} = l^{3-C_3}$ with:

$$C_3 = C_2 \frac{3}{d_{el}} \tag{3.1}$$

where d_{el} is the "elliptical" dimension of the rain process characterizing the stratification, estimated (Lovejoy et al., 1987) to have the value $d_{el}=2.22\pm0.07$ in rain (d_{el} would be three if the space was isotropic, and two if it was completely stratified into flat layers). Using eq. 3.1, and expressing n in terms of the volume $\upsilon = l^3$ we obtain:

$$\langle n(\upsilon)\rangle \propto \upsilon^{(1-C_2/d_{el})} \tag{3.2}$$

Hence, using the above values of C_2, d_{el} in eq. 3.2 the drop density $\langle n(\upsilon)\rangle/\upsilon$ is no longer constant as demanded by Poisson statistics, but decreases as $\upsilon^{-0.08}$.

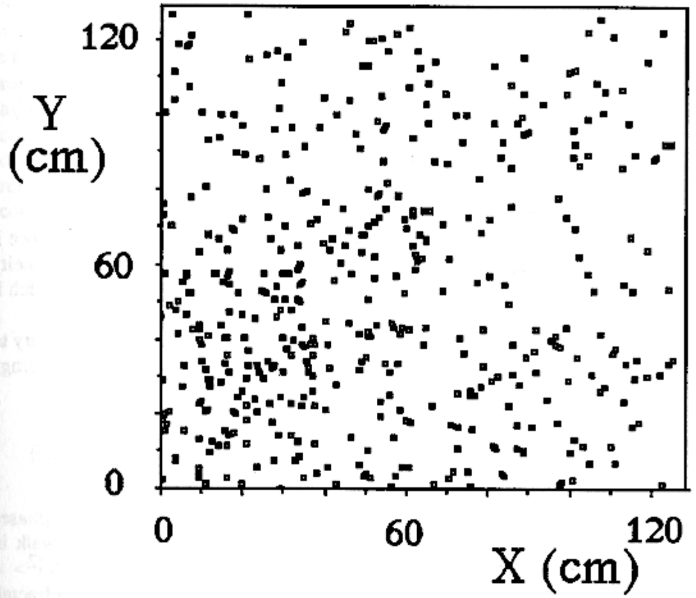

Fig. 3.1: Each point represented the centre of a raindrop for the 128X128 cm piece of chemically treated blotting paper discussed in the text. There are 452 points, the exposure was about 1s.

The effect of this drop clustering on radar signals will be to introduce some degree of coherent scattering from the drops. To quantify this, consider a radar at the origin that emits a pulse of electromagnetic waves with wavevector $\underline{k}$, that fills a volume $\upsilon = l \times r\theta \times r\theta$ where r is the range, θ the angular width of the radar beam, l is the pulse length. The power recieved at the radar depends on various instrumental characteristics including the transmitter, antenna geometry etc. Putting these factors into a multiplicative constant (ignored below) and statistically averaging (indicated by angle brackets), the radar measures the "effective radar reflectivity factor" (Z_e) whose statistical average (indicated by the brackets "< >") is:

$$\langle Z_e\rangle \propto \frac{\langle |A|^2\rangle}{\upsilon} \tag{3.3}$$

Where

$$A = \sum_{j}^{n(\upsilon)} V_j e^{i2\underline{k}\cdot\underline{r}_j} \tag{3.4}$$

and $\underline{r}_j$ is the position vector of the jth drop and the factor 2 arises because the beam makes a round trip.

Therefore, accoring to eq. 3.3, 3.4, the radar measures the square of the modulus of the Fourier component of the drop distribution (weighted by the drop volumes) at wavevector $\underline{k}$. We therefore calculate the Fourier transform ($Z_e(\underline{k})$), and plot (fig. 3.3) the angularly and radially integrated quantity

$$|\underline{k}|^{-2} \int_{S|\underline{k}|} Z_e(\underline{k}')\, d^2\underline{k}' \propto |\underline{k}|^{\zeta} \tag{3.5}$$

where $S_{|\underline{k}|}$ is the circle of radius $|\underline{k}|$ and empirically, we find $\zeta \approx -0.12$ (we integrate over circles in Fourier space in eq. 3.5 to take advantage of the presumed statistical horizontal isotropy of the drop distribution). The factor $|\underline{k}|^{-2}$ was included so that white noise (Poisson statistics) will yield $\zeta=0$, and deviations from white noise will be easy to see. $|\underline{k}|$ was varied over the range $\frac{2\pi}{128}50\ \mathrm{cm}^{-1} \geq |\underline{k}| \geq \frac{2\pi}{128}\mathrm{cm}^{-1}$ (which corresponds to the range 2 - 128 cm). Only extremely small deviations from this behaviour can be noted at high wavenumbers corresponding to about 4cm. The clustering (correlations) of the drops lead to coherent scattering, thus for a given wavenumber, there is an increase in Fourier amplitudes, hence a decrease in ζ as compared to white noise.

3.2. Estimating range dependent biases in radar reflectivities

Before continuing with our analysis of this data, it is worth pursuing the Fourier result a bit further, since it introduces corrections into the standard theory of radar measurements of rain which assume homogeneity (white noise). The calculation of the corrections to the standard theory is quite simple, so that we sketch it below.

We have already introduced the “effective radar reflectivity factor” (eq. 3.3, 3.4). It is customary to introduce the "radar reflectivity factor" (usually measured in units of $\mathrm{mm}^6/\mathrm{m}^3$) whose ensemble average $\langle Z \rangle$ is defined by:

$$\langle Z \rangle = \frac{\langle n(\upsilon) \rangle}{\upsilon} \langle V^2 \rangle \tag{3.6}$$

If the drops are uniformly randomly distributed (i.e. they have Poisson statistics), the phases $2\underline{k}\cdot\underline{r}_j = \phi_j$ in eq. 3.4 are statistically independent. Considering the complex sum A as a random walk in phase space, as long as $\langle V^2 \rangle < \infty$ the central limit theorem applied to (3.4) implies: $\langle |A|^2 \rangle = \langle n(\upsilon) \rangle \langle V^2 \rangle$ and hence the classical result $\langle Z_e \rangle = \langle Z \rangle$. However, if the drops are distributed over a fractal, we have partially coherent scattering and we expect drop correlations to yield an anomalous exponent:

$$\langle |A|^2 \rangle \propto \langle n(\upsilon) \rangle^{2H} \langle V^2 \rangle \tag{3.7}$$

where H=1/2 for completely incoherent scattering, and H≠1/2 when some degree of coherent scattering is present. Hence:

$$\langle Z_e \rangle \propto \langle Z \rangle \langle n(\upsilon) \rangle^{2H-1} \tag{3.8}$$

In order to evaluate H from the blotting paper we used the following procedure. First, in order to reduce statistical scatter, we take $|\underline{k}|$ fixed and exploit the statistical isotropy of the drops in the horizontal by averaging over wavevectors in 19 equally spaced directions, adding more and more terms in the sum (A) by choosing drops at random from the 452 available. Fig. 3.4 shows that convergence to a power law is obtained for $n \geq 16$. Varying $|\underline{k}|$ in 10 equal logarithmic increments through the scaling region, from $\frac{2\pi}{128}\mathrm{cm}^{-1}$ to $\frac{2\pi}{1.28}\mathrm{cm}^{-1}$ (corresponding to distances of 1.28 to 128cm), we obtained $2H = 1.24 \pm 0.09$ where the error is the standard deviation of the 2H values estimated from each of the values of $|\underline{k}|$.

We can now combine this result with our previous formula (3.2) for $n(\upsilon)$ to obtain the volume (and hence range) dependence of $\langle Z \rangle$, $\langle Z_e \rangle$. Recalling that $\upsilon = l\theta^2 r^2$ and keeping only the r dependence, combining eq. 3.2, 3.6, 3.8, and using the notation $\langle Z \rangle \propto r^{\xi}$, $\langle Z_e \rangle \propto r^{\xi_e}$ we obtain:

$$\xi = -\frac{2C_2}{d_{el}} \tag{3.9}$$

$$\xi_e = 4H\left(1 - \frac{C_2}{d_{el}}\right) - 2$$

Taking $C_2 \approx 0.17$, $H=0.62$, $d_{el}=2.22$ yields $\xi = -0.15$, $\xi_e = 0.28$ (recall that the standard values are $C_2=0$, $H=1/2$, $d_{el}=3$, hence $\xi=\xi_e=0$). To judge the overall magnitude of these effects, consider a weather radar such as the 10cm wavelength one at McGill, with minimum range (limited by ground echoes) of ≈10km, and maximum range ≈240km. Comparing near and far range, we obtain a variation in $\langle Z_e \rangle$ of $\approx 24^{0.28} \approx 2.4$, and a corresponding variation in $\langle Z \rangle$ of $24^{-0.15} = 0.6$. These effects are somewhat larger in magnitude than those due to absorption (by humidity, O_2, and by the drops themselves) and should be taken into account during radar calibration from rain gages. However, more study is needed since the above corrections do not fully take into account the scaling proerties of rain. They could be termed “monofractal” corrections since they involve a small number of paramters (H,C), and yield corrections for the mean reflectivity factor. In Lovejoy and Schertzer (1990c), we discuss other (multifractal) corrections which correct the higher order moments (or equivalently, the probability distributions via corrections to $c(\gamma)$).

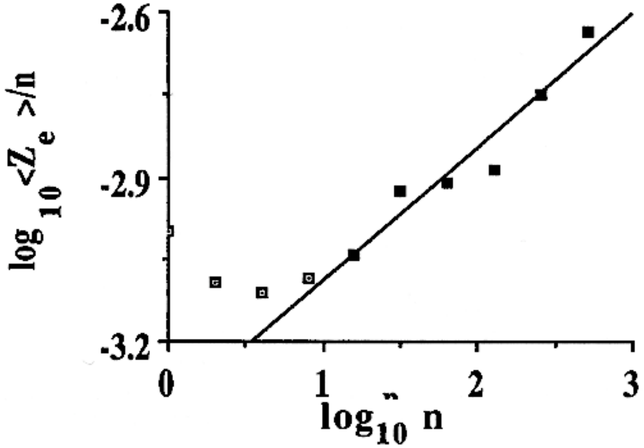

Fig. 3.4: The variation of the mean (non-dimensionalised) reflective radar reflectivity of the distribution in fig. 3.1 normalized by the number of drops (n) used in calculating the sum (eq. 3.3, 3.4), as a function of the number of drops (n). The curve is calculated as indicated in the text and involves averaging over 19 angles in Fourier space, and 10 logarithmically space wavelengths from 1-128cm. The straightline shows the asymptotic power law behaviour which is obtained for $n \geq 16$, with slope = 2H-1 = 0.24 (H = 0.62). Note that white noise (Poisson statistics) would yield a flat curve (slope zero, H = 1/2). The increase is due to some degree of coherent scattering.

3.3. Trace moment analysis

Physical applications of scaling typically involve scaling functions (or measures) rather than sets (see Schertzer and Lovejoy (1987a,b) for more detailed discussion). In spite of this, the traditional emphasis has been on fractal sets and their dimensions, even though it requires us to first transform the measure into a set (e.g. by thresholding) and then to construct Hausdorff measures from the set by covering it with "balls". As argued earlier, it is more natural to to treat the fractal measure directly; we do this by introducing a series of measures (introduced in Schertzer and Lovejoy, 1987a,b), called "trace moments". This approach is similar to that of Hentschel and Proccacia (1983), Grassberger (1983), Halsey et al. (1986). For an early application of the same technique to rain (including an empirical evaluation the codimension function in rain), see Schertzer and Lovejoy (1985b) where it is refered to there as an "integral structure function".

We again cover the set S (dimension D) with disjoint boxes B_λ, scale λ (diameter $l = L/\lambda$, L again being the largest scale of interest). We then "homogenize" f over the various B_λ's writing:

$$f_\lambda = \frac{\int_{B_\lambda} f(\underline{r})\, d^D\underline{r}}{\lambda^{-D}} \tag{3.10}$$

f_λ is the "homogenized" ("smoothed") f over B_λ used in section 2 (the denominator λ^{-D} is proportional to the area (D=2), volume (D=3) etc. of B_λ). Rather than study the effect of smoothing on the probability distributions of f_λ (characterised by $c(\gamma)$), we can study its effect on the moments of different orders:

$$\langle f_\lambda^{\,h}\rangle \approx \lambda^{(h-1)C(h)} \tag{3.11}$$

Where the "< >" indicates ensemble averaging. The equality holds when f_λ has been normalized so that $\langle f_\lambda\rangle=1$, otherwise the symbol "≈" in eq. 3.11 indicates proportionality. The exponent $(h-1)C(h)$ quantifies the rate at which the various moments are smoothed with decreasing λ (increasing *l*). As long as the statistical moments converge, a box-counting approximation allows C(h) to be interpreted as a codimension function for the moments (not to be confused with $c(\gamma)$). This can be seen by introducing a Hausdorff measure called an "hth order trace moment[1], resolution λ, of f over S" denoted: $\langle Tr_\lambda f(S)^h\rangle$:

$$\langle Tr_\lambda f(S)^h\rangle \approx \sum_i^{N(\lambda)} \langle f_\lambda^{\,h}\rangle (\mathrm{diam} B_\lambda)^h \approx \lambda^D \lambda^{(h-1)C(h)-hD} \approx \lambda^{(h-1)d(h)} \approx \lambda^{-K_D(h)} \tag{3.12}$$

since in the above the sum is approximated by multiplication by $N(\lambda)\approx\lambda^D$ and:

$$\langle f_\lambda^{\,h}\rangle (\mathrm{diam} B_\lambda)^h = \langle \left(\int_{B_\lambda} f(\underline{r})\, d^D\underline{r} \right)^h \rangle \tag{3.13}$$

the trace moments $\langle Tr_\lambda f(S)^h\rangle$ can therefore be estimated by the statistical moments of f spatially integrated over boxes of size L/λ. We then estimate the exponent $K_D(h)$ (= $-(h-1)d(h)$, $d(h)=D-C(h)$) by studying the scaling of the latter.

Furthermore, C(h) is a dual codimension function related to $c(\gamma)$ via a Legendre transformation:

$$c(\gamma) = \min_h \left(h\gamma - (h-1)C(h)\right) \tag{3.14}$$

3.4. Trace moments for drop volume and probability measures

We may now use eq. 3.12 to estimate $K_D(h)$ for the blotting paper $(V_i, \underline{r}_i)$ rain measure. Two measures with obvious physical significance are: $f_V=(V_i, \underline{r}_i)$ and $f_n=(1, \underline{r}_i)$ where

$$\int_S f_V(\underline{r})\, d^D\underline{r} = \text{the total amount of water in S} \tag{3.15}$$

and

$$\int_S f_n(\underline{r})\, d^D\underline{r} = \text{the total number of drops in S} \tag{3.16}$$

---

[1] The "≈" sign on the left of eq. 3.12 is introduced because the covering yielding the "infimum" in the Hausdorff measure defining the trace moment has been approximated by a covering of N(λ) disjoint boxes - see the discussion of the box-counting approximation in appendix B.

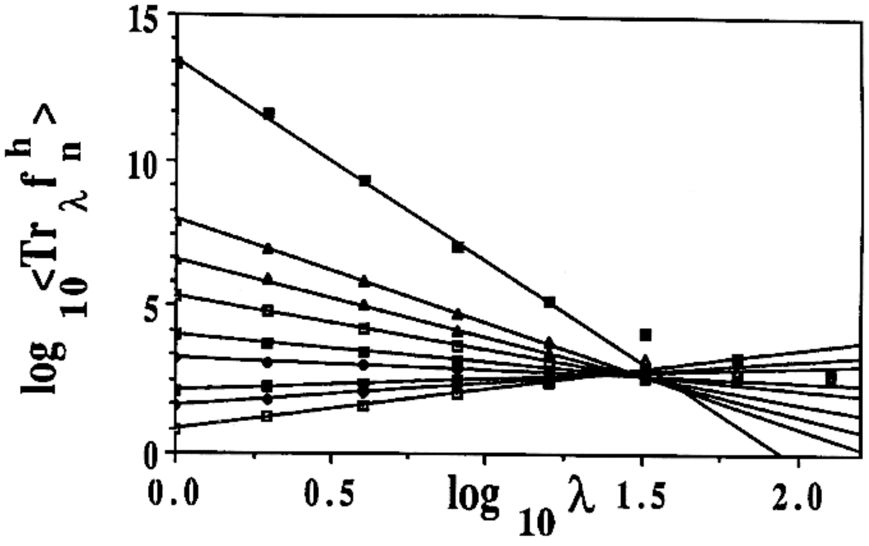

Fig. 3.5a: A log-log plot of the (unnormalized) $\langle Tr_\lambda f_n^{\,h}\rangle$ which is proportional to $\lambda^{-K_{nD}(h)}$ v.s. λ=L/*l* where λ is the scale ratio, L the external size (=128cm), *l* the size of homogeneity and f_n is the number measure discussed in the text. Note that *l*=128 cm and that convergence to power laws occurs only for lengths *l*≥4cm (λ<32). The curves, top to bottom, are for h = 5, 3, 2.5, 2, 1.5, 1.2, 0.8, 0.6, 0.3, and the (negative) slopoes are the corresponding values of the function $K_{nD}(h)$. Straight lines were fit for *l*≥8cm.

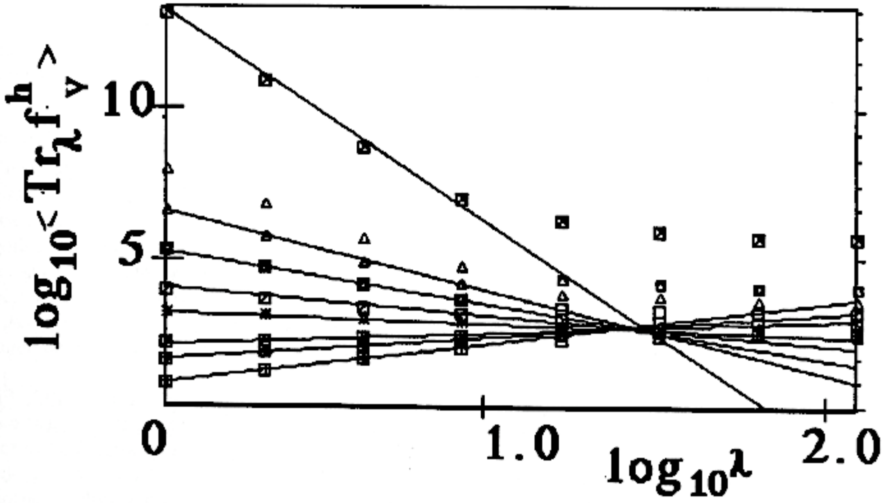

Fig. 3.5b: Same as 3.5a but for the volume measure discussed in the text. Straight lines fitted for *l*≥8cm.

The latter is simply an (non-)normalized probability measure f_p.

We first examine $K_{nD}(h)$ (the number measure scaling exponent function), since it is the simplest characterization of $(V_i, \underline{r}_i)$; it is equivalent to studying the set of drop centres only. In our case, it has the further advantage of being the only measure obtained from more than one rain event. In addition to the 452 drop event described in section 3.1, we manually analysed two other events (with 1293, and 339 drops respectively), obtaining $K_{nD}(h)$ for $h>0$.

All exposures were for ≈ 1s, fig. 3.5a, b shows a typically plot of $\log\langle Tr_{\lambda} f(S)^h\rangle / \langle Tr_{\lambda_s} f(S)^h\rangle$ vs. $\log\lambda$ with λ ranging from 1 to 128. We find that for $l \geq 8$cm that scaling is fairly well respected. The change in behaviour for $l \leq 4$cm is due to the fact that many drops per resolution element are required to obtain asymptotic scaling properties. This hypothesis was supported by an analysis of the two other cases which showed that the break does not occur at a fixed scale, but rather at a fixed (average) number of drops per box of about 16. This is consistent with the results in fig. 3.4 showing that roughly 16 drops are required to reach the asymptotic scaling behaviour.

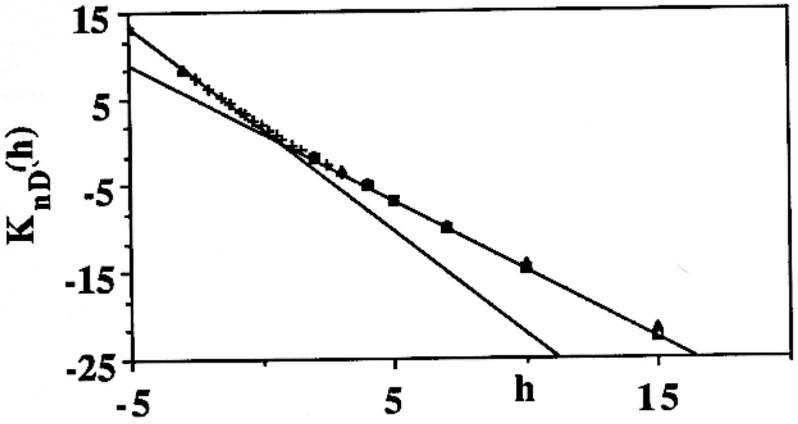

Fig. 3.6: $K_{nD}(h)$ estimated from (bottom to top) a manually analysed 1293 drop case ($h>0$ only), the 452 drop (digital) case analysed in fig. 3.5, and a 339 drop manually analysed case ($h>0$). The straight lines are asymptotic fits to the negative and positive large (absolute) h regions for the 452 drop case, yielding (absolute) slopes $D_{-\infty} = 4.06$ and $D_{\infty} = 1.56$.

Fitting the trace moments for $l \geq 4$cm, we obtained excellent fits. Fig. 3.6 shows $K_{nD}(h)$ for the three cases indicating that $K_{nD}(h)$ is curved at small absolute h, but fairly straight for large absolute h. This type of asymptotic straight-line behaviour was also found for radar reflectivities in Schertzer and Lovejoy (1987a). Theoretically, this behaviour (at least for positive h) can arise from a number of sources, including perhaps the divergence of high order statistical moments, and a resulting spurious scaling (see Lavallée et al. this volume for discussion). Denoting the small h and large h asymptotic (absolute) slopes by $D_{-\infty}$ and D_{∞}.respectively, we obtain D_{∞} for the 1293 drop case, =1.79, for the 452 drop case =1.56, and for the 339 drop case, =1.51. $D_{-\infty}$ was only evaluated in the digitised 452 drop case, yielding 4.064. Note that in the latter case, $K(2)=D_2 \approx 1.83$ which agrees as expected with the value of the correlation dimension found in section 3.1.

Next, we evaluated $K_{VD}(h)$ in the 452 drop case, obtaining results very similar to $K_{nD}(h)$. Fig. 3.7 shows $K_{VD}(h)$ in this case evaluated for $l \geq 8$cm. The similarity of this curve with the $K_{nD}(h)$ curve is compatible with a very low degree of correlation between drop clustering and drop size. To test this, we evaluated yet another, "randomized" measure that we obtained by replacing V_i in $(V_i, \underline{r}_i)$ by a V_i' obtained by choosing V_i at random from the V_i in the sample. Fig. 3.7 shows that except for very large absolute h, the functions $K_{VD}(h)$ and $K_{V'D}(h)$ are nearly the same. The large h behaviour does appear to be somewhat different however, since the (randomized) asymptotic absolute slope of $K_{V'D}(h)$ yielded $D_{\infty} = 1.47 \pm 0.03$ while that of the (unrandomized) $K_{VD}(h)$ yielded $D_{\infty} = 1.56$. We interpret this as indicating that correlations between drop position and size are most important for the larger drops (since they contribute most to the higher moments).

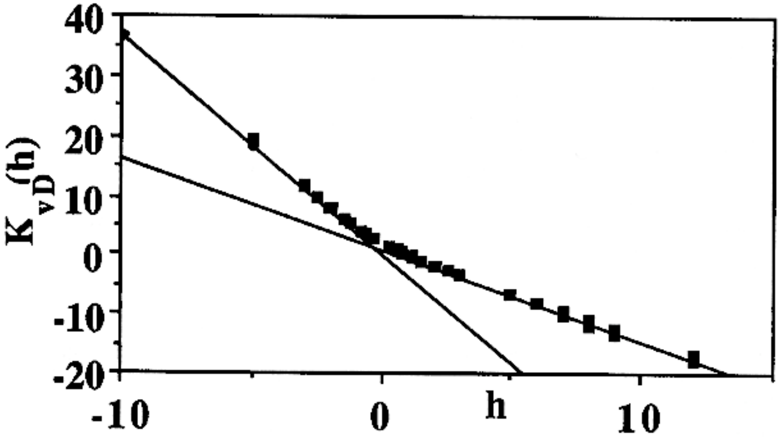

Fig. 3.7: $K_{VD}(h)$ for the 452 drop case (lower curves) and $K_{V'D}(h)$ for two randomized cases discussed in the text (upper curves). The straight lines are asymptotic fits to the negative and positive large (absolute) h regions for the 452 drop case, yielding for $K_{VD}(h)$, $D_{-\infty} = 3.65$, $D_{\infty} = 1.56$.

4. LIDAR MEASUREMENTS OF RAIN DROPS

4.1. Extending the blotting paper results in time and space

In an attempt to extend the blotting paper results of section 3 to much greater time and space scales, we undertook to examine the reflexions of high-powered laser pulses (lidar) from rain drops. Lidar has generally been used to detect very small particles (such as aerosols) whose tiny size (typically <1µm) precludes their measurement by microwaves. Even with high power and telescopic receivers, the return signal is typically very weak and relatively long pulse lengths (e.g. 50m) and averages over many repeated pulses are used to improve the signal to noise ratio. Lidars have also been used to study clouds, where the drops are typically 1-20µm in size. Here the problem has not been the weakness of the return signal, but rather the high density and efficiency of the scatterers which attenuates the signal so strongly that typically only the cloud edge is detected.

Our approach was somewhat different. By studying large drops (rain-typically 0.5-3mm in diameter), with high power and short range, we can obtain excellent signal to noise ratios, even with very small pulse lengths (here ≈ 3m) and averaging over pulses is not required (of course, the measurements had to be performed after dark). Also, unlike the typical lidar configuration in which the beam is directed upwards, here, we pointed it in the horizontal. Furthermore, the lower density of rain drops as compared to cloud drops means that attenuation is not a serious problem. Although an ultimate objective is to reduce the pulse length to centimetres or smaller (lasers with these characteristics are readily available), and to measure the position and reflection of individual drops, our electronics were insufficiently fast. The set-up involved a YaG laser with 10ns pulse duration (0.1J per pulse, at 10Hz) with a frequency doubler so that it emitted in the green region of the spectrum. Although the pulse volume is too large to isolate individual drops completely unambiguously (due to beam spreading, the pulse volume at a 10m distance is 20cm^3, while at 1km, it is 0.2m^3) the return signal still yields valuable information on the time/space structure of rain. The experiment (including the assembly of the laser, telescope, photomultiplier and triggering circuits) was performed by Alex Powell and John Weisnagel, as part of their 3rd year honours physics lab project.

The data were digitised and archived on floppy disks in two basic formats, the overall limitation being the floppy disk capacity. In the first format, the object was to produce roughly square (x,t) plots so that 180 consecutive pulses were stored (0.1s between pulses) with a downrange resolution of 180 pulse lengths (=180X3=540m). In the second format, much longer series of pulses were available (5000 over a period of 5000X0.1=500s), but over only a couple of pulse lengths. Other data sets obtained included (z,t) experiments where z is the vertical coordinate. We expect systematic analysis of these data sets to yield not only information on the multiple scaling of rain over these small time and space scales, but also on the statistical anisotropy of (x,y,z,t) space. This is important since the hypothesis of the isotropy of (x,y,z,t) space constitutes a statistical version of the well-known Taylor hypothesis of "frozen turbulence" which is often invoked but which has not been directly tested[1]. In the following, we give only preliminary results which over the range of scales studied, confirm the scaling in both space and time. These are however, consistent with a generalization of Taylor's hypothesis of frozen turbulence in which the space and time scales are statistically the same if one of the axes is differentially stratified (compressed) with respect to the other.

4.2. Data analysis and results

An example of the raw data photomultiplier voltage (in light rain) is shown in fig. 4.1. The basic features to note are a) the steep rise in the first 50m, b) the steady power law fall-off of the mean signal. The initial rise is due to the telescope focusing effect (the close range was out of focus), while the fall-off, roughly following r^{-4} law, is expected for single particle scattering (if there is no attenuation, then the outgoing signal falls off as r^{-2}, similarly for the reflected signal).

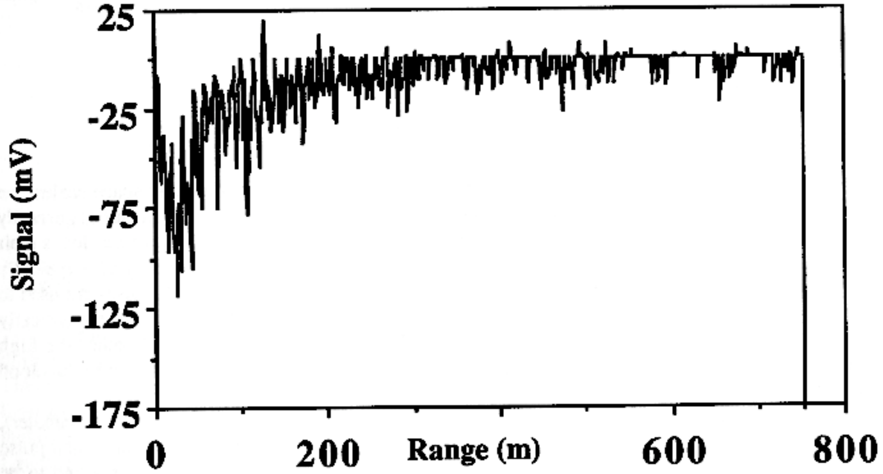

Fig. 4.1: An example of an uncorrected lidar pulse return. The reflected intensity is measured by the magnitude of the (negative) photomultiplier voltage (in millivolts). Note the initial dip in the signal due to poor telescope focus at near range, as well as the fairly rapid (r^{-4}) fall-off further downrange. Positive values are due to electronic noise and must be reset to zero. The far range rerurn is from a distant apartment building.

To remove both of these obvious range dependencies, we eliminated all data closer than 50m, and applied a simple r^4 correction. A perspective plot of a typical (range corrected) sequence of pulse returns, as is shown in fig 4.2, indicating that there is no longer any obvious range dependence. In fact, a subtle range effect must still exist because as the pulse spreads away from the lidar, there is a tendency for the pulse volume to include more and more drops, and hence increase the signal. Apparently, this effect has been somewhat offset by a decrease due to some attenuation. In any case, we do not expect these effects to yield a serious bias in our analyses since the same mix of near and far data was used in trace moments estimated at each scale. This is the same argument as that used in Lovejoy et al. (1987) with regard to the effect of the spreading of the radar beam.

---

[1] See appendix E for discussion.

4.3. Trace moment estimates of correlation dimensions

Although the pulse volume is generally too large to lead to completely unambiguous conclusions about number and size of the drops in a pulse volume, it was still small enough that at light rain rates, many of the pulse volumes gave very low return signals (signals compatible with either aerosol scattering or other noise sources this is true of most of the return signals with voltage ≥ 0 in 4.1). There was therefore some indication that by putting a fairly low threshold on the return signal, that a crude separation could be made into rain and no-rain pulse volumes. In the following, we therefore analyse only the set of pulse volumes exceeding the sample average signal. The properties of this set were then investigated by the trace moment analysis described in section 4.3.

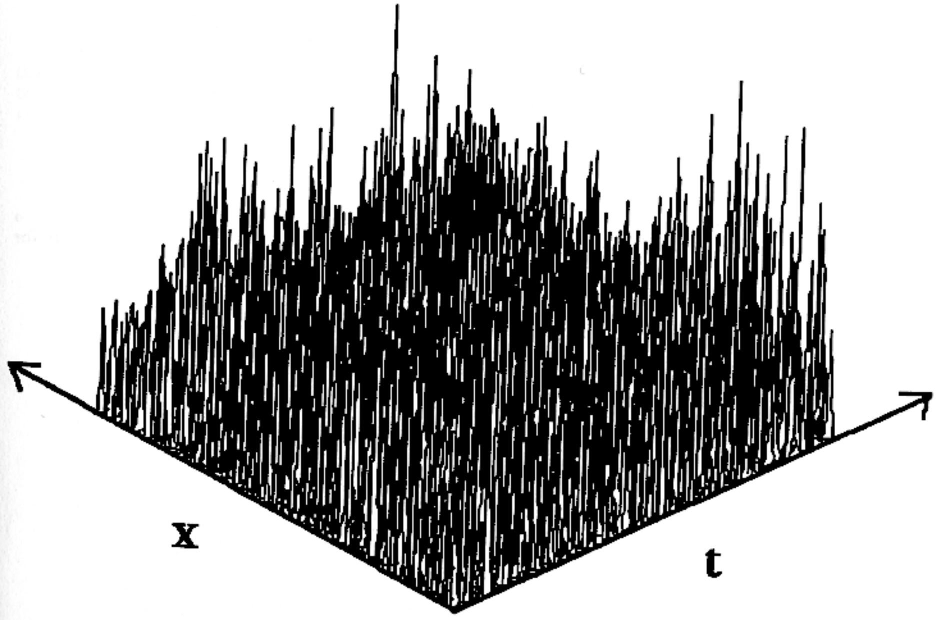

Fig. 4.2: A (x,t) perspective plot of the log of the absolute (range corrected) lidar reflectivity (vertical coordinate) indicating the extreme variation, in both space and time, as well as the approximate absence of remaining range biases (180X180 points are shown).

Fig. 4.3 shows such an analysis on a time sequence involving 5000 pulses (=500s). The telescope was focused at near range allowing pulse volumes only 10m from the lidar to be studied. At this range, these were 0.3mm in diameter and therefore sufficiently small so that often no scattering took place. In this case, due to the proximity - the scattering occured in a McGill parking lot - the above statement could be readily verified by eye: at a given range reflections occured only at fairly irregular intervals. In fig. 4.3, note how accurately the scaling is followed. Using the slopes to estimate $K_D(h)$, and the formula $d(h) = -K_D(h)/(h-1)$ we find that the dimensions of these 1-D sequences were typically in the range

0.9-0.85. The resulting codimensions (0.1 - 0.15) are comparable to those found in section 4.1 for the (x,y) distribution (0.17) but a proper analysis of the difference in space/time codimensions has not yet been performed, however, the results here are sufficient to conclude that space and time do not scale in the same way - see appendix E for a theoretical discussion.

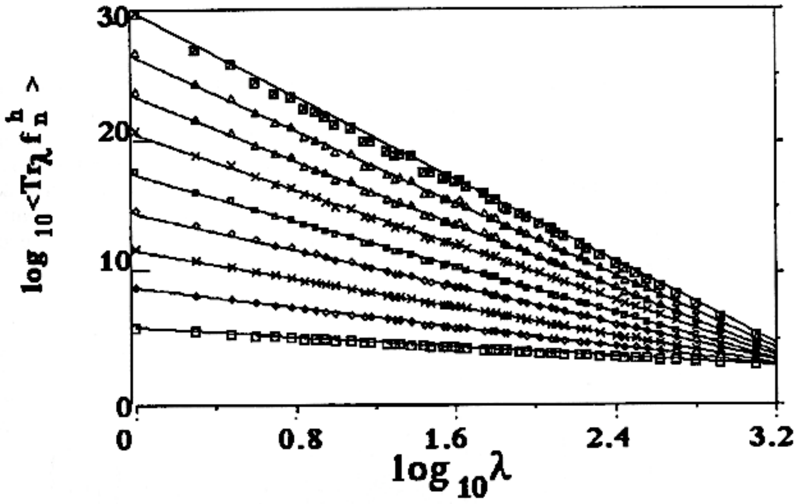

Fig. 4.3: Trace moment analysis (similar to that in figs. 3.5a,b) for the time domain (5000 pulses over a period of t_0=500s) for those range corrected returns that exceeded the average. Curves from top to bottom are for h=10, 9, 8, 7, 6, 5, 4, 3, 2 respectively. Note that the scaling is extremely accurately followed.

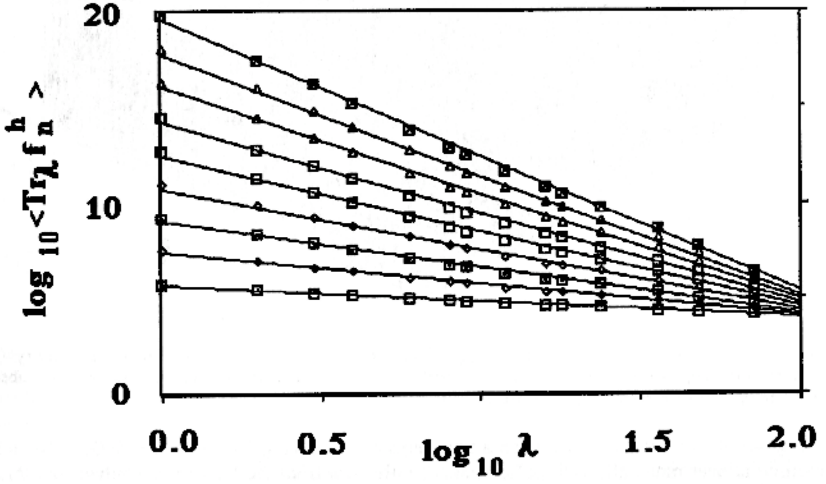

Fig. 4.4: Trace moment analysis for downrange domain (each pulse return is divided into 180 pulselength sections, 3m apart (L=540m) for those range corrected returns that exceeded the average. Curves from top to bottom same as for fig. 4.3. Note that the scaling is extremely accurately followed.

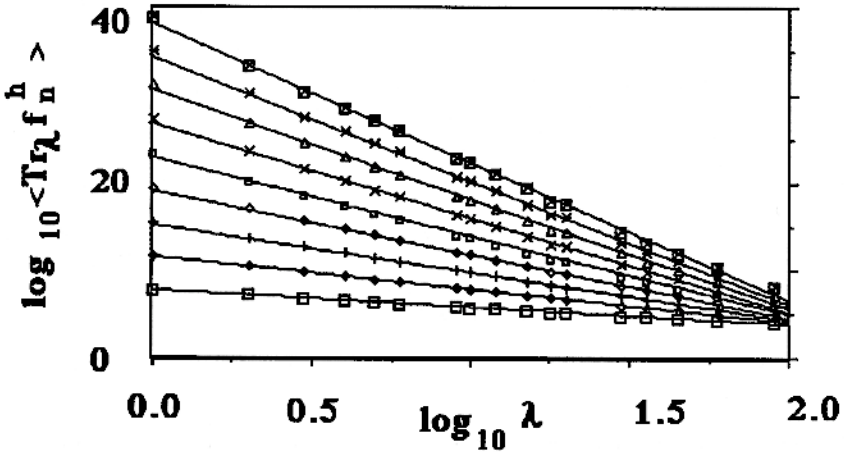

Fig. 4.5: Trace moment analysis for the (x,t) domain (180 pulses, 0.1s apart in time, space resolution 3m) for those range corrected returns that exceeded the average. Curves from top to bottom same as for fig. 4.3. Note that the scaling is extremely accurately followed. This data set is the same as that shown in fig. 4.4, except that analysis was performed on "squares" in (x,t) space rather than by intervals (downrange) only.

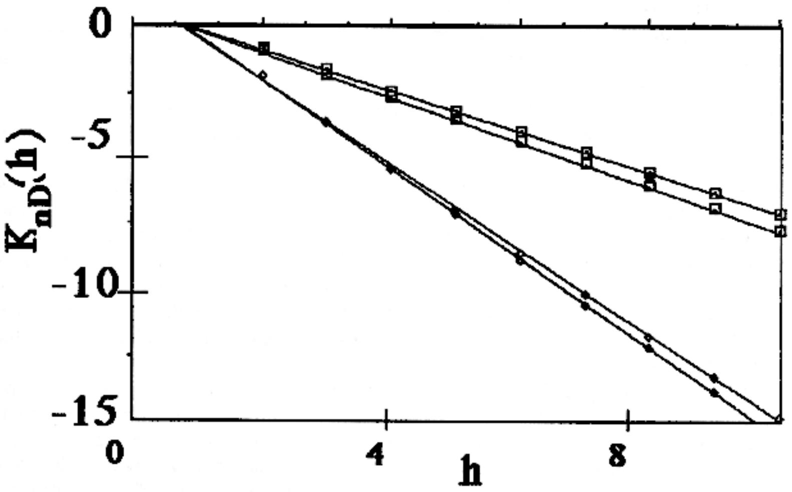

Fig. 4.6: Comparisons of the functions $K_{nD}(h)$ obtained (bottom to top) from lidar (x,t space), blotting paper (x,y space) lidar (t space), lidar (x space). The two upper lines are steeper because they are embedded in a two dimensional space, while the lower lines in a one dimensional space.

In fig. 4.4 we analyse down-range returns for another storm, using the r^4 correction and again thresholding at the sample averaged threshold. Again, the scaling is accurately followed over the entire range of scales from 3 to 540m, with similar dimensions. Fig. 4.5 shows the results for the 180X180 (x,t) field described above, again showing the scaling. Fig.4.6 compares the functions $K_{nD}(h)$ obtained from 3.5a, 4.3, 4.4, 4.5 yielding estimates of D_∞ = 1.56 (x,y, blotting paper), 1.68 (x,t, lidar), 0.84 (t, lidar), 0.76 (x, lidar), or, $C_\infty = 0.44, 0.32, 0.16, 0.24$ respectively. These results are not immediately comparable since both the data sets and measurement methods were different (for example, if the x,y space is statistically isotropic, then from a theorem on intersections, $C_\infty(x,y)= C_\infty(x)$). More can be said about the lidar (x) and (x,t) space results since in this case, the same data set was used. The difference between $C_\infty(x)$ and $C_\infty(x,t)$ (0.24 and 0.32 respectively) - if confirmed in more detailed studies- indicates that an anisotropic version of Taylor's hypothesis holds. A preliminary estimate of the elliptical dimension of the (x,t) space is: $d_{elx,t} = 2\times0.24/0.32= 1.5\pm0.3$ where the (large) error is estimated by assuming that the individual errors in the estimates of C_∞ is ±0.03. This result is consistent with space-time transformation involving turbulent velocities yield $d_{elx,t} \approx 5/3$.

Combining the blotting paper results (several mm- ≈1m fig. 4.2), the lidar results (≈3m - 0.5km, figs. 4.4, 4.5), with satellite analyses (≈100m-100km, fig. A.2, and ≈8 - 512km, fig. 2.1) we we have an excellent indication of the existence of a continuous multiple scaling structure of rain and clouds over nearly the entire range of meteorologically significant space scales.

5. CONCLUSIONS

The object of this paper has been to discuss and illustrate new data analysis techniques which directly analyse multifractal measures, determining the codimension function characterizing the singularities of various orders (the PDMS technique), as well as a related (dual) codimension function characterizing the scaling of the various statistical moments (the trace moment technique). Unlike ("mono-fractal") methods adapted to studying the geometric properties of sets (which involve single fractal dimensions), both methods involve creating a series of lower resolution fields and allow direct determination of the entire (co)-dimension function. Since geophysical phenomena are typically measures (or fields when averaged over the resolution of a sensor), mono-fractal techniques operate by first transforming the fields into sets, typically by applying thresholds. This indirect procedure is unsatisfactory since the values of the thresholds depend fundamentally on the resolution of the sensor; in appendix A we re-examine several of the most commonly used mono-fractal techniques (particularly area-perimeter relations and area distribution exponents[1]) in this context. We then apply these multifractal techniques to infra red and visible satellite surface and cloud radiances, radar reflectivities of rain, blotting paper data on rain-drop size and position, and lidar data on the space-time structure of raindrops.

In section 2, we applied the Probability Distribution/Multiple Scaling (PDMS) technique showing how it could be used to establish the multiple scaling of satellite cloud and surface radiances in visible and infra-red wavelengths and determine the resolution independent (normalized) probability distribution (the codimension function). We further showed how this function fits into theoretically predicted universality classes, estimating the important parameters characterizing the generators of the process. This is important since it helps both to justify and to calibrate, the modelling of clouds by continuous cascade process (c.f. Wilson et al. this volume). The PDMS technique is appealing because of its simplicity, and the fact that it directly corresponds to a systematic degradation of the data resolution.

In section 3, we directly studied the (V_i, r_i) (= volume, position) measure defined by raindrops as they intersected a large piece of blotting paper. Using a variety of techniques including Fourier analysis and trace moments, we were able to not only establish the multiple scaling of the measure, but also to quantitatively evaluate systematic corrections that the behaviour will introduce into radar reflectivities. The corrections arise due to the long-range correlations in rain associated with its multifractal structure. On the one hand, these correlations lead to a degree of coherent scattering that enhances the radar signal above its conventionally assumed level. On the other hand, the sparseness of the raindrops leads to a decrease in their density with scale which tends to act in the opposite sense. Quantitative evaluation of the relative

---

[1] The re-evaluation of the mono-dimensional techniques involved a number of new findings. First, that the area-perimeter exponent will not in general be the dimension of the perimeter, but rather the ratio of the perimeter dimension to half the dimension of the area (in appendix A- we empirically show that this correction is often of the order of 25% or more). Second, the distribution of areas has an exponent which is generally expected to be <1, since unlike many simple geometric fractal sets, in fractal measures, we do not expect fragmentation of structures, to play a very important role in determining the fractal dimensions (appendix D).

importance of the two effects shows that it is the former which dominates, yielding a systematic bias that may easily reach 50% in typical weather radar systems.

The blotting paper analysis was unfortunately too limited to permit more systematic investigation of the rain structure- particularly due to the lack of vertical resolution and small sample sizes. This limitation prompted the final study reported here, which involved very short pulselength lidar (laser) measurements of rain drops. Although we could not completely unambiguously distinguish pulse volumes with one or more drop from those without any, an approximate separation was achieved showing that over the range 0.1s to 500s, and 3 - 540m, in space, that the distribution of raindrops is scaling. We also evaluated the multiple fractal dimensions of the set of rain-filled pulse volumes. Although these results are preliminary, they clearly established the scaling in this important range of time/space scales. If we combine the analyses of section 2,3,4 and appendix A (not to mention quite a few other analyses in the literature), we find a convincing case for the multiple scaling of rain and clouds over the entire range of millimeters to nearly a thousand kilometers.

In light of these findings, we can affirm that the only convincingly documented evidence of scale breaking to date is at the viscous scale (≤1 mm) and at planetary scales (≥1000km). However, as with any theoretical idea, no amount of empirical evidence could ever prove the validity of the scaling hypothesis. However, the lack of strong evidence for breaks in the scaling means that the latter- if they exist- are likely to be relatively weak. This evidence, coupled with theoretical arguments in favour of such scaling -not to mention its unifying and simplifying power- certainly make the hypothesis more attractive than ever.

6. ACKNOWLEDGMENTS

We acknowledge discussions with, G.L. Austin, A. Davis, P. Gabriel, J.P. Kahane, P. Ladoy, D. Lavallée, E. Levich, A. Seed, A.A. Tsonis, R. Viswanathan, J. Wilson.

APPENDIX A: THRESHOLDING AND MULTIFRACTAL MEASURES: A RE-EVALUATION OF SEVERAL MONO-DIMENSIONAL ANALYSIS TECHNIQUES

A.1. Discussion

We have argued (especially in section 2), that emphasis on the geometric properties of scale invariant processes has lead to excessive emphasis on the study of sets, and their fractal dimensions. For example, using a threshold on satellite cloud and radar rain data, Lovejoy (1981, 1982) determined area-perimeter and area-distribution exponents. Although limited to the range 1-1000km, and to a single cloud and rain intensity level and meteorological situation, Lovejoy (1982) showed that scaling could hold over a wide range of meteorologically significant length scales. Since then, these and related methods have been used by a number of other investigators (e.g. Carter et al., 1986; Ludwig and Nitz, 1986; Rhys and Waldvogel, 1986; Welch et al., 1988; and several authors in this volume), occasionally yielding apparently contradictory results. For example, the value of the area-perimeter exponent of 1.35 found in Lovejoy (1982) was at first considered a fundamental constant, which was subsequently found to be not always reproducible; Rhys and Waldvogel (1986) and Cahalan (this volume) found generally higher values that depended on the realization ("meteorological situation"), and Carter et al. (1986) estimated the dimension of the "graph" of infra red radiance intensity from clouds, obtaining yet another value of the dimension. However, once the multifractal nature of the fields is appreciated, these results can be easily explained. In particular, the interpretation and significance of the area-perimeter and area distribution exponents, graph dimensions, as well as their relationship to the fractal dimensions of the rain or cloud regions themselves must be re-examined. This is done below; the most important results are a) the area-perimeter exponent will in general not be equal to the fractal dimension of perimeter b) the range of possible values and significance of the area distribution exponent is different than that obtained by simple arguments on geometric sets. We then re-examine these early studies in this multifractal context.

A.2. Multifractal exceedance sets, perimeter sets and graphs

Consider the function $f_\lambda(\underline{r})$ obtained by averaging a multifractal measure over scale l, scale ratio λ, in a region of the plane[1] $\Re$ size $R \times R$ (i.e. with large scale $L=R$). As mentioned in section 2, the underlying measure is most directly studied by considering how the properties of f vary as we change λ (e.g. by successively degrading our sensor resolution). However most applications of remotely sensed data involve studying the properties of f_λ at fixed λ. When, as is often the case, these exponents are obtained by using thresholds (T_λ) on f_λ to define sets, we find that the results will depend directly on λ via the multifractal relation $T_\lambda = T_1 \lambda^\gamma$ where T_1 is the large (e.g. image scale resolution) value of the field (T_1 is at the same resolution as f_1). Our exponents will therefore depend (via T_λ) on both the sensor resolution (λ), and the "meteorlogical situation" (i.e. stochastic realization) of the process, and hence be of limited utility. Below, we fix the function resolution λ, and write simply $f(\underline{r})$, T.

Define the (closed) exceedance set $S_{T\geq}$ as the set of points satisfying $f(\underline{r}) \geq T$. If $f(\underline{r})$ is a scaling function, the (Hausdorff) dimension $D(S_{T\geq})$ of $S_{T\geq}$ will be a nonincreasing function of T, since $S_{T\geq} \supset S_{T'\geq}$ for T'>T and the dimension of a subset must ≤ to the dimension of the entire set (this property is so basic that it holds for all definitions of dimension of which we are aware, including topological dimensions)[2].

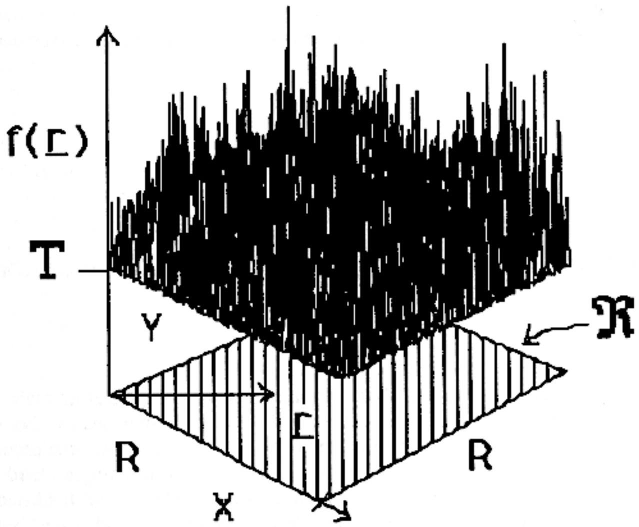

Fig. A.1a: Schematic illustration showing some of the definitions used in the text. G_T is the set of points in the black (spiky) region above the plane $f(\underline{r})=T$.

Consider next the "graph" (G) of $f(\underline{r})$ defined as those points in three dimensional ($\underline{r}$, $f(\underline{r})$) space. As before, we may define G_T as the subset of G such that $f(\underline{r}) \geq T$ (see fig. A.1 for an illustration, and appendix D for more discussion). Consider now the perimeter set of $S_{T\geq}$, denoted p_T. p_T is the "border set" of $S_{T\geq}$, more properly defined as the "T-crossing set" of G with the plane $f(\underline{r})=T$ (in analogy with the expression "zero-crossing" used in the theory of stochastic processes). This is the set of points $\underline{r}$ such that arbitrarily small neighbourhoods of $\underline{r}$ contain some points such that $f(\underline{r})<T$ and some such that $f(\underline{r}) \geq T$. Using basic notions about sets, we can now give a definition of p_T. Define the (open) complement of $S_{T\geq}$ as: $\bar{S}_{T\geq} = \Re - S_{T\geq}$. p_T is thus the set of "contact" points of $\bar{S}_{T\geq}$ which are required to close it, yielding $[\bar{S}_{T\geq}]$. We thus obtain:

---

[1] Generalizations to higher dimensional spaces are straightforward and will not be explicitly considered.

[2] Complications arising from non-self-similar, anisotropic scaling (Generalized Scale Invariance, see e.g. Schertzer and Lovejoy, 1987), will not be considered here.

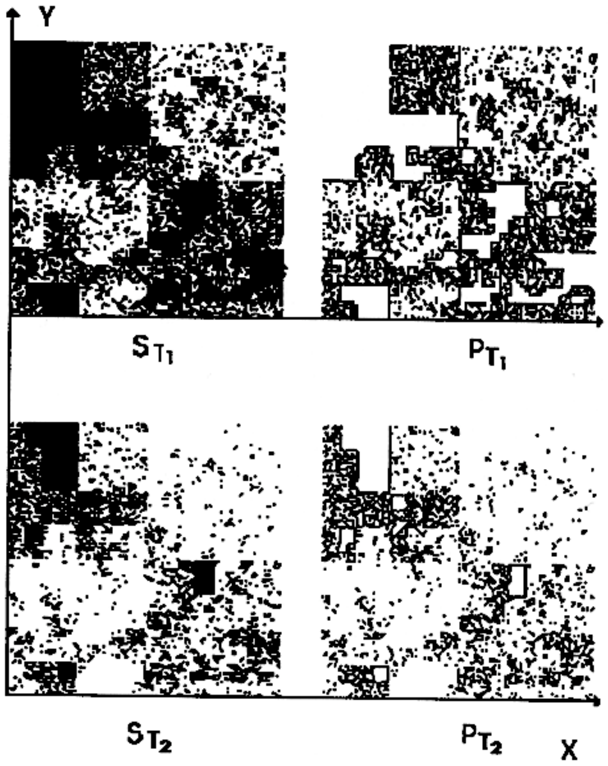

Fig. A.1b: Schematic illustration showing the definition of $S_{T\geq}$, p_T used in the text, for two different thresholds $T_1 < T_2$. The illustration was produced using a multiplicative cascade process (an "alpha model") with a cascade discretised into 8 steps of a factor two in scale each step.

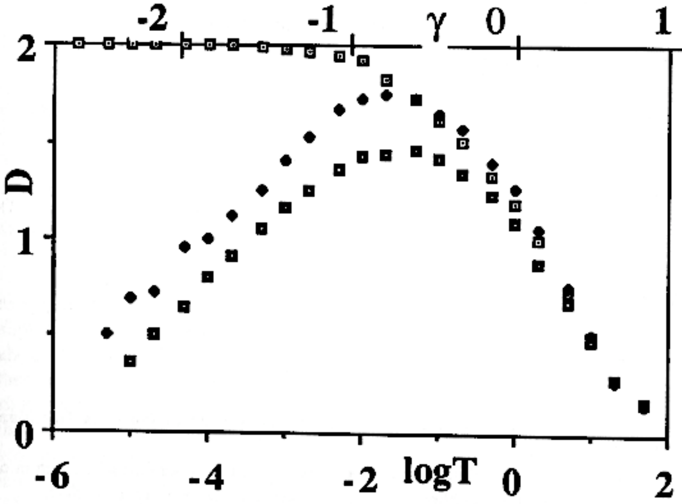

Fig. A.1c: Graph of the functions $D(S_{T\geq})$ (white squares), $D(p_T)$ (diamonds), $D(S_{T=})$ (black squares) determined numerically from a multiplicative cascade process on a 128X128 point grid. As expected, the functions respect the inequality A.2.

$$p_T = [\bar{S}_{T\geq}] \cap S_{T\geq} \tag{A.1}$$

It is important not to confuse this zero-crossing set with the set of points $\underline{r}$ such that $f(\underline{r})=T$ which is the intersection of G with the plane $f(\underline{r})=T$, $(G \cap T)$ denoted $S_{T=}$. In general, p_T will be different from $S_{T=}$ with the two coinciding only if special conditions apply such as G is everywhere continuous (i.e. G typically jumps from one side of the plane $f(\underline{r})=T$ without intersecting it[1]). However, in what follows, we see that in general, G is discontinuous, and all we obtain is:

$$D(S_{T\geq}) \geq D(p_T) \tag{A.2}$$

(since $S_{T\geq} \supset p_T$) with the actual value of $D(p_T)$ however depending critically on the topological structure (i.e. connectedness) of the set. Fig. A.1c compares the functions $D(S_{T\geq})$, $D(p_T)$, $D(S_{T=})$ for a numerical simulation of a multifractal cascade process on a 128X128 point grid (mean=1), with Gaussian generator (except for the extreme fluctuations, the intensities are log-normally distributed - see Lavallée et al. (this volume) for more details). The dimensions were estimated using the box-counting technique described in appendix B[2]. In order to get a large enough sample size to estimate the dimension function $D(S_{T=})$, the latter was estimated from the sets $S_{T+\Delta T\geq}$-$S_{T>}$ with $\Delta T=0.2T$.

Note that as $T \to \infty$, $D(S_{T\geq})$ can $\to D_\infty > 0$ (this occurs for example in the "α model", Schertzer and Lovejoy (1983,1985)), although in general[3] (especially in continuous cascades), we expect $D_\infty = 0$. In the latter (more general) case $D(p_T)$ may initially increase with T, although it must eventually decrease.

A.3. The relation between $D(P_T)$ and area-perimeter exponents

We can now relate the areas and perimeters by eliminating R in the above equations. Using box-counting to estimate the Hausdorff dimensions (see appendix A), we obtain:

$$N_s(r) \approx \left(\frac{R}{r}\right)^{D(S_{T\geq})} \tag{A.3}$$

$$N_p(r) \approx \left(\frac{R}{r}\right)^{D(p_T)}$$

where N is the number of rXr boxes required to cover the set (which is of linear size R).

The areas $A_T(r)$ and perimeters $P_T(r)$ are given by:

$$A_T(r) = N_s(r) r^2 = \left(\frac{R}{r}\right)^{D(S_{T\geq})} r^2 \tag{A.4}$$

$$P_T(r) = N_p(r) r = \left(\frac{R}{r}\right)^{D(p_T)} r$$

eliminating R, we obtain:

$$P_T = A_T^{D(p_T)/D(S_{T\geq})}\, r^{1-2D(p_T)/D(S_{T\geq})} \tag{A.5}$$

or:

---

[1] $p_T = G \cap T$ does however generally apply to the mono-dimensional processes (such as fractional Brownian motion) discussed in Mandelbrot (1982).

[2] The procedure of transforming f_L into sets with threshold L, and measuring the dimension as a function of T using box-counting, constitutes the functional box-counting technique discussed in Lovejoy et al. (1987).

[3] See Schertzer and Lovejoy (1987a, this volume), for a discussion of this point, including universality classes of $D(S_{T\geq})$.

$$P \propto (\sqrt{A})^{\xi_T}\, r^{1-\xi_T} \tag{A.6}$$

where $\xi_T = 2D(p_T)/D(S_{T\geq})$. When $D(S_T)=2$ (i.e. the exceedance sets are not fractal), we obtain $\xi_T = D(p_T)$ which is the relationship discussed in Mandelbrot (1982), and applied to cloud areas in Lovejoy (1982). Alternatively, using the value ξ_T rather than $D(p_T)$ we are in error by the ratio $2/D(S_{T\geq}) \geq 1$.

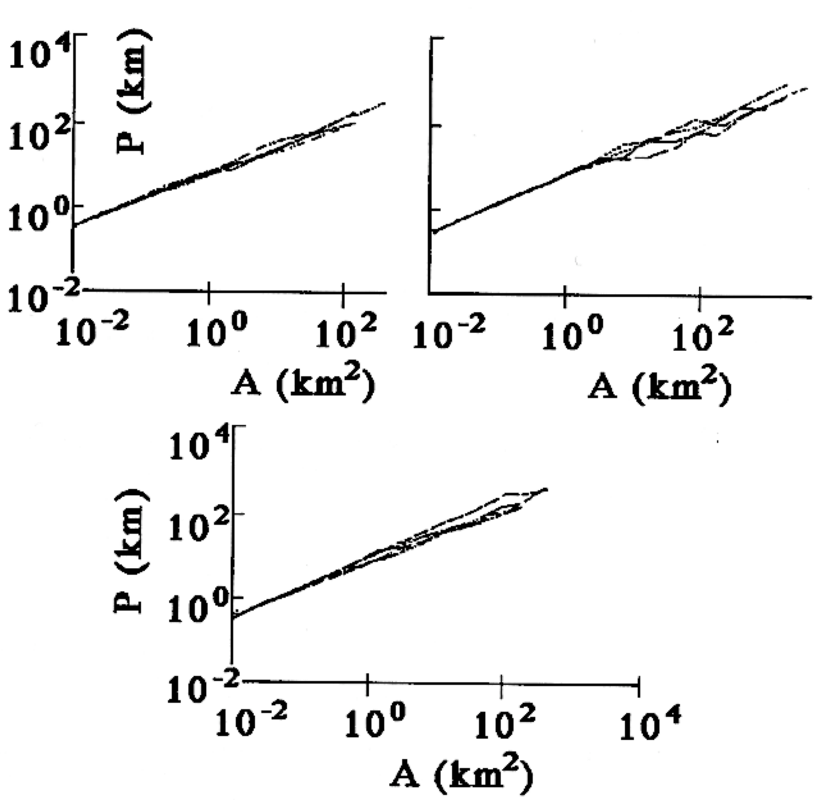

Fig. A.2: Area-perimeter curves for 9 different LANDSAT scenes (28m resolution) replotted from Welch et al. (1988). Although, as expected, different scenes yield different slopes, there is no evidence for a break in the scaling over the entire range of 10^{-2} to (nearly) 10^4km^2.

Recently, Welch et al. (1988) have used the same method to analyse LANDSAT data with 28m resolution to study visible cloud radiance fields. Although the authors claim that two straight lines with slightly different slopes (what they call "bifractal" behaviour) can be fit to their graphs (with a break at about 1km^2), single straight lines (one for each scene) do excellent jobs, as readers may verify for themselves (see fig. A.2 reproduced from their fig. 8). In any case, since the latter applied their analyses to single scenes, there will be statistical fluctuations due to the finite sample size. Furthermore, basic theoretical ideas about multifracals (as well as cascade simulations performed in Lavallée et al. (this volume)) indicate that for multifractal fields fluctuations are generally likely to be very large (strong intermittency) for individual realizations. In any case, it would be interesting (following Gabriel et al. (1988)) for the authors to reanalyse their data to try (for each scene seperately) to statistically reject the hypothesis that individual straight provide good fits. For the moment, we interpret these data as giving strong support for the scaling of cloud radiance perimeters between 10^{-2} and 10^4 km^2 for a variety of cloud types (i.e. precisely through the range of 1km^2 where Cahalan (this volume) claims evidence for a break).

The above analysis shows that we should not be surprised by the empirical finding that area-perimeter relations give fairly constant exponents typically in the range $1.3 \leq \xi_T \leq 1.6$, since both $D(p_T)$ and $D(S_T)$ are likely to decrease slowly with increasing T, and hence the ratio $\frac{D(p_T)}{D(S_T)}$ may be expected to remain relatively fixed (see Yano and Takeushi (this volume) and Cahalan (this volume); the latter finds a slight increase of ξ_T with T, yielding typical low (dim) cloud values of 1.5, and high (bright) cloud values of 1.6). Note that this correction is not negligible; empirically, we find (Gabriel et al., 1988) that even for very low values of T, that $D(S_T) \approx 1.8$ at both visible and infra red wavelengths, and may easily decrease to ≈ 1.5 for very bright regions or cold tops. These values lead to corrections of 1.11 and 1.33 respectively. Applying these to Cahalan's typical range of ξ_T values we obtain $D(p_T) \approx 1.35$ and 1.20 respectively.

A.4. Other implications of multifractals for analysis methods

The preceding sub-sections have shown that multifractal fields are generally considerably more difficult to analyse than their monodimensional counterparts. Two other techniques that have been used to study scaling in cloud fields are area distribution exponents and the dimensions of graphs. Both techniques must be applied with considerable care to multifractal fields. In the former case (discussed in detail in appendix C) the interpretation of the exponents is quite different for multi and monofractals. In the latter (appendix D), shortcuts in performing box-counting that assume continuity of the process (which holds in many common monofractal processes but not generally in multifractal ones) can (and do) lead to completely erroneous results

Another aspect of multifractals that must be carefully considered in analysing data, is that unlike the monodimensional case, the thresholds that correspond to a given fractal dimension depend directly on the resolution with which the basic fractal measure is averaged by the measuring device. Even if the resolution is constant, the dimension corresponding to a given threshold will also depend on the realization of the process (e.g. the "meteorological situation"). As argued earlier, this difference between mono and multifractal processes is very basic; for now, we briefly discuss how these new dependencies can lead to practical difficulties, including apparent breaks in the scaling symmetry.

i) Pooling data from different realizations: Pooling data (e.g. in box counting, in area-perimeter graphs, or in area histograms) is a useful way of increasing sample size to obtain better statistical estimates of the parameters. However, it must be performed very carefully in multifractal fields, since it can "mix" fractals with different dimensions. For example, Rhys and Waldvogel (1986) consider area-perimeter relations obtained by pooling areas and perimeters of radar rain areas over consecutive images in time, using the same threshold. Since the dimensions for the fixed threshold will in general vary in time, this mixes fractals with different dimensions. If the sample was large enough, this would not be serious, since the largest area-perimeter exponent would eventually dominate the rest. However, if the fractals have nearly the same dimensions (as they do in their study), the convergence is extremely slow, and finite samples, will yield either large spreads or non-linear log-log plots, that can easily (and erroneously) be interpreted as breaks in the scaling. These results must therefore be re-analysed before any conclusions about symmetry breaking can be drawn.

ii) Combining spatial averaging with thresholding: The variation of fractal dimension with threshold can lead to artificial symmetry breaking in yet another way. Consider taking a short-cut in estimating areas and dimensions by fixing a threshold and degrading successively the resolution of the set which exceeds the threshold (e.g. by box-counting), calculating p_T from the set at different resolutions. This method will work whether or not the field is multifractal, since it is first converted into a set having a well defined dimension. However, if rather than degrading the set resolution, we degrade the multifractal field itself by simply averaging the field (rather than the set) over larger and larger scales, and then defining the exceedance set with respect to the previous threshold (as in Yano and Takeuchi, this volume), the method will no longer work. To recuperate a set with the same dimension, the threshold must be appropriately decreased to compensate for the fact that averaging over larger scales decreases (smooths) the intense regions (the precise amount of decrease can be quantitatively estimated by associating each threshold with singularities as in the following section). As long as sufficiently low thresholds are used so that the dimension varies relatively little with threshold (i.e. in this range of thresholds, the field is approximately mono-dimensional), this effect will not be too important, but at extreme threshold levels, where the dimension changes more rapidly with threshold (e.g. for the cirrus clouds in Yano and Takeuchi, this volume) this will yield systematic (but totally artificial) breaks in the scaling (the downward curvature observed in their curves).

APPENDIX B: ESTIMATING HAUSDORFF DIMENSIONS BY BOX-COUNTING:

Box-counting techniques have been developed for some time to estimate the dimension of strange attractors and other fractal sets. Lovejoy et al. (1987) showed how it could be applied to multifractal fields by transforming them into the series of sets $S_{T\geq}$ as indicated above.

Box counting arises as a natural method for estimating Hausdorff dimensions. This may be seen by recalling the definition of Hausdorff measures and dimensions. Consider a set (fractal or otherwise) S. Define the "Hausdorff measure of S resolution l relative to the (convex) function g" as follows:

$$\mu_{l,g}(S) = \inf_{\text{all coverings } B_i \text{ such that diam } B_i \leq l} \sum_{i}^{N(l)} g(\mathrm{diam}(B_i)) \tag{B.1}$$

where we cover the set with $N(l)$ "balls" B_i of diameter = diam(B_i) such that diam(B_i)$\leq l$. The "inf" is over all possible coverings and is responsible for the practical difficulties in evaluating Hausdorff measures. Next, we define the "Hausdorff measure of S relative to g" as:

$$\mu_g(S) = \lim_{l \to 0} \mu_{l,g}(S) \tag{B.2}$$

Next, taking $g(t)=t^h$, we can define the "h-dimensional Hausdorff measure of S", $\mu_h(S)$. Finally, we can define the "Hausdorff dimension" (D(S)) as:

$$D(S) = \inf_h (\mu_h(S)=0) = \sup_h (\mu_h(S)=\infty) \tag{B.3}$$

The (non-trivial and extremely general) equality between the inf and the sup (which implies a brutal transition from 0 to ∞ as h is decreased below D(S)), is the property that makes Hausdorff dimensions so useful, since they can be applied to virtually any set. The interpretation of the above property is straightforward. For example, when applied to a planar set S (D(S))=2), it says that the "volume ($\mu_3(S)$)=0, and that the "length" ($\mu_1(S)$)=∞. The size of the set is then given by $\mu_{D(S)}(S)$ (which for standard sets, yields the Lebesgue measure of S as expected). Note that some sets (such as the trail of a Brownian particle, which, when embedded in a space with $d \geq 2$, has D(S)=2), yields $\mu_{D(S)}(S)=0$ even though the set has an infinite number of points. These are "marginal" sets and require using $g(t)=t^{D(S)}(\log t)^{\delta 1}(\log\log t)^{\delta 2}\cdots$ with at least one of the δ's>0. These are the source of the "log corrections" that are sometimes discussed in this context. Note that Mauldin and William (1986) have shown that in a certain class of random fractal sets, that log-correction arise quite naturally. It is therefore perhaps not too surprising that in some cases where the trace moments indicate that power law scaling is well respected (e.g. the lidar data discussed in section 5), that simple box-counting yields curved log $N(l)$ v.s. log l plots compatible with log corrections.

The box-counting approximation is now relatively simple to describe. Ignoring the possibility of logarithmic corrections, (i.e. taking $g(t)=t^h$), and covering the set with disjoint "cubical" balls, size l, so that diam(B_i)=l (i.e a regular grid, discarding the inf), we obtain:

$$\mu_{l,h}(S) \approx \sum_{i=1}^{N_S(l)} l^h = l^h N_S(l) \tag{B.4}$$

taking the limit $l \to 0$, and recalling that $\mu_h(S)$ is finite and non-zero only if $h=D(S)$, we obtain:

$$N_S(l) \approx l^{-D(S)} \qquad \text{as } l \to 0 \tag{B.5}$$

which yields the estimate:

$$D(S) = \lim_{l \to 0} -\frac{\log N_S(l)}{\log l} \tag{B.6}$$

APPENDIX C: AREA DISTRIBUTION EXPONENTS

Consider the problem of relating the distribution of contiguous areas equal to or exceeding T to the set $S_{T\geq}$. If $D(S_{T\geq}) > 1$ then $S_{T\geq}$ will generally be made up of many contiguous subsets (denoted $s_{T\geq}^{(i)}$) each with external scale Λ_i for the i^{th} region. Because of the assumed scaling, the Λ will generally be distributed (to within logarithmic corrections) as:

$$Nr(\Lambda > l) \propto l^{-B_T} \tag{C.1}$$

where "Nr" indicates the number of subsets $s_{T\geq}^{(i)}$ whose size exceeds l. Note that since $S_{T\geq} \supset s_{T\geq}$, $D(s_{T\geq}) \leq D(S_{T\geq})$.

At resolution r, a subset $s_{T\geq}$ with scale l will have area:

$$a_T(r) \approx \left(\frac{l}{r}\right)^{D(s_{T\geq})} r^2 \tag{C.2}$$

Hence, eliminating l in terms of a_T, we obtain:

$$Nr(A_T > a_T) \propto a_T^{-B'_T} \tag{C.3}$$

where $B'_T = B_T/D(s_{T\geq})$. Empirically, B'_T is the most readily accessible area exponent. Lovejoy (1981, and Lovejoy and Mandelbrot (1985) show empirically that for light rain rates, low clouds, $B'_T \approx 0.75$. Lovejoy and Mandelbrot (1985) and Lovejoy and Schertzer (1985) also develop mono-dimensional models with B'_T in the range 0.5 - 0.75. Another reference is Cahalan (this volume) who obtains $B'_T \approx 0.8$ for satellite cloud pictures.

We now seek to relate B_T, $D(s_{T\geq})$ and $D(S_{T\geq})$. To do so, note that the total number of boxes required to cover S_T is:

$$N_S(r) \approx \left(\frac{R}{r}\right)^{D(S_{T\geq})} \propto \int_r^R \left(\frac{l}{r}\right)^{D(s_{T\geq})} dNr(\Lambda > l) \tag{C.4}$$

where $dNr(\Lambda > l) \propto l^{-B_T-1}dl$ is the number density associated with $Nr(\Lambda > l)$. The above yields:

$$N_S(r) \propto r^{-D(s_{T\geq})} \int_r^R l^{D(s_{T\geq})} l^{-B_T-1} dl \tag{C.5}$$

taking into account the sign of $D(s_T)-B_T$, this yields

$$N_S(r) \propto r^{-D(s_{T\geq})} \left[\left| R^{D(s_{T\geq})-B_T} - r^{D(s_{T\geq})-B_T} \right| \right] \tag{C.6}$$

The relative values of $D(s_{T\geq})$ and B_T depends on the topological (connectedness) properties of the process. We must now distinguish two cases depending on which is greater:

i) $B_T \geq D(s_{T\geq})$: In this case, in the limit $r \to 0$, the $r^{D(s_{T\geq})-B_T}$ term dominates the $R^{D(s_{T\geq})-B_T}$ term and the number of boxes/subset is small compared to the total number; fragmentation dominates, and:

$$N_S(r) \propto r^{-B_T} \qquad \Rightarrow \qquad B_T = D(S_{T\geq}) \tag{C.7}$$

This is the case discussed in Mandelbrot (1982) where geometric generators are used to produce fractal sets which yield $D(s_{T\geq}) < D(S_{T\geq})$. We therefore have $D(S_{T\geq}) = B_T > D(s_{T\geq}) \Rightarrow B'_T = \frac{B_T}{D(s_{T\geq})} > 1$.

ii) $B < D(s_{T\geq})$: In this case, in the limit $r \to 0$, $R^{D(s_{T\geq})-B_T}$ dominates $r^{D(s_{T\geq})-B_T}$ and the number of boxes/fractal subset is a large fraction of the total; the number of boxes needed to cover the fragments is negligible compared to the number needed to cover individual connected regions, this yields:

$$N_S(r) \propto r^{-D(s_{T\geq})} \qquad \Rightarrow \qquad D(s_{T\geq}) = D(S_{T\geq}) \tag{C.8}$$

and $B_T < D(s_{T\geq})$ and hence $B'_T = \frac{B_T}{D(s_{T\geq})} < 1$. Each contiguous region has the same dimension as the entire set, and the fragmentation is relatively unimportant. This is the case relevant to multifractal fields, and of interest in geophysical applications.

APPENDIX D: GRAPHS AND THEIR DIMENSIONS

Carter et al. (1986) considered the x-z cross-section (intersection) of the graph G of the infra red cloud radiance as a function of telescope scanning angle (for clarity we use the notation $(\underline{r}, f(\underline{r})) = (x,y,z)$ since $\underline{r} = (x,y)$ and f=z=radiance, x,y are angle variables). Denote this intersection set by $G \cap (xz)$. They then estimate the dimension of G using box-counting to cover the graph of $G \cap (xz)$. However, their method actually implicitly assumes continuity- they use additional boxes to cover not only their experimental points, but also those points on straight lines connecting the latter. Their resulting estimate of $D(G \cap (xz))$ is very near 1 (1.16, and 1.11 depending on the wavelength used), and we may therefore suspect that it is an artifact of their assumption of continuity (since the connecting straight lines have dimension 1, while the experimental points have D<1, their method will estimate the maximum of the two). We now discuss this possibility in more detail.

The simplest way to relate $D(G_T)$ to $D(S_{T\geq})$ and $D(S_{T=})$ is recall that $S_{T\geq}$ is the projection of G_T with the x,y plane. The projection set (S_p) of S_1 onto S_2 has dimension:

$$D(S_p) = \min(D(S_1), D(S_2)) \tag{D.1}$$

in this case, we obtain:

$$D(S_{T\geq}) = \min(D(G_T), 2) \tag{D.2}$$

There are now two distinct possibilities:

i) $D(S_{T\geq}) = 2$:

If the process is non-stationary, such as the (mono-dimensional, Gaussian) fractal Brownian motion processes used by Mandelbrot (1982) and Voss (1983) to model mountains, then the graph is continuous (but non-differentiable), but rarely crosses the plane $f(\underline{r})=T$, and $D(S_{T\geq})=2$, and the projection relation gives us no further information about $D(G_T)$.

ii) $D(S_{T\geq})\leq 2$:

The process is stationary (as are cascade processes, and, presumably most remotely sensed fields), in this case, we will generally have $D(S_{T\geq})<2$, hence the projection relation yields:

$$D(G_T)=D(S_{T\geq})<2 \tag{D.3}$$

In this case (which applies to the examples shown in fig. A.1a,b,c), G_T will be discontinuous everywhere. We now consider $G\cap(xz)$ studied by Carter et al. 1986. All the preceeding results apply to $G\cap(xz)$, $S_{T\geq}\cap(xz)$ etc., as long as the dimensions of all the above sets are reduced by one (if the corresponding value becomes negative, it must be reset to zero). Since we have empirical evidence that generally, $D(S_{T\geq})<2$ (see the section 2), we expect $D(S_{T\geq})=D(G_T)$, so that $D(G_T\cap(xz)) = D(S_{T\geq}\cap(xz))<1$, implying that $G\cap(xz)$ is discontinuous everywhere. However, Carter et al. (1986) assumed that $G\cap(xz)$ was continuous, and effectively interpolated their experimental points with a continuous line (dimension 1 which is $> D(G\cap(xz))$), hence we expect them to obtain an estimate D=1 (the maximum of the dimension of the set of points on $G\cap(xz)$ and the set on the line connecting them). Indeed, careful inspection of the Carter et al. (1986) box-counting figures ($N(l)$ v.s. l) indicate that the function $N(l) \approx l^{-1}$ (hence D=1) fits well over most of the range of l (which was only over roughly two orders of magnitude anyway).

This example, illustrates the dangers of approaching the data analysis with, unwarranted theoretical preconceptions about the continuity of the process.

APPENDIX E: Generalized scale invariance and space-time transformation in rain:

In both geophysical and laboratory flows, it is generally far easier to obtain high temporal resolution velocity data at one or only a few points than to obtain detailed spatial information at a given instant. It is therefore tempting to relate time and space properties by assuming that the flow pattern is frozen and is simply blown past the sensors at a fixed velocity without appreciable evolution, and to directly use the time series information to deduce the spatial structure. This "Taylor's hypothesis of frozen turbulence" (Taylor, 1938) can often be justified because in many experimental set ups, the flow pattern is caused by external forcing at a well defined velocity typically much larger than the fluctuations under study. However, in geophysical systems (in particular in the atmosphere and ocean) where no external forcing velocity exists, the hypothesis has often been justified by appeal to a meso-scale gap separating large scale motions (e.g. "weather") and small scale "turbulence". If such a separation existed, it might at least justify a statistical version of Taylor's hypothesis in which a the large scale velocity is considered statistically constant (stationary). Various statistical properties such as spatial and temporal energy spectra would be similar even though no detailed transformation of a given time series to a particular spatial pattern would be possible. Only some kind of statistical equivalence could be made.

If, as argued in this paper and in many of the references cited in the introduction, the meso-scale gap is a fiction, then no large scale forcing velocity can be appealed to in order to transform from space to time, and turbulent velocities must be used instead of amplitude $v_l \approx \langle\varepsilon_l^{1/3}\rangle l^{1/3}$ where l is the scale of the eddy, ε_l is the energy flux through the eddy to smaller scales. Although $\langle\varepsilon_l\rangle$ is scale independent, due to intermittency[1] $\langle\varepsilon_l^{1/3}\rangle \approx l^{\delta}$ where δ is a small correction. Rather than being scale independent, the space-time transformation has a scale dependent velocity[2] $v_l \approx l^H$ with $H \approx 1/3+\delta$. The two geophysically relevant Taylor's hypotheses therefore correspond to H=0 or $H=1/3+\delta$ depending on the existence (or not) of the "gap".

The theoretical arguments mentioned above make it clear that the turbulent velocity is likely to be relevant one for space-time transformations, and the clear differences in slope in the trace moments analyses

---

[1] These are due to multifractal effects, the exact value of will depend on the $K_D(h)$ function for the velocity field, as well as on which value of h is relevant for rain.

[2] Each moment of the rain field will require a different δ. For simplicity, we ignore this complication here.

(figs 4.3-4.5) rule out the constant velocity (H=0) hypothesis[1]. The space-time transformation we infer from the turbulent value of H ($\approx 1/3$) can be easily expressed in the formalism of Generalized Scale Invariance. Consider (x,y,t) space, the space-time transformation can be simply expressed by statistical invariance with respect to the following transformation: $x \to x/\lambda$, $y \to y/\lambda$, $t \to t/\lambda^{1-H}$ or using the notation $\underline{r}=(x,y,t)$, $\underline{r}_\lambda = T_\lambda \underline{r}_1$ with $T_\lambda = \lambda^{-G}$ and:

$$G = \begin{bmatrix} 1 & 0 & 0 \\ 0 & 1 & 0 \\ 0 & 0 & 1-H \end{bmatrix};$$

we therefore obtain Trace(G)= 3-H, i.e. by measuring d_{el} or H we can determine G (assuming that there are no off-diagonal elements corresponding to rotation between space and time, and ignoring differential rotation in the horizontal). The isotropic statistical Taylor's hypothesis[2] is $H \approx 1/3$, $d_{el} \approx 8/3$. If we now consider the full (x,y,z,t) space, it has already been shown (Lovejoy et al., 1987) that $d_{el} \approx 2.22$ for the corresponding transformation in (x,y,z) space for radar rain data, hence, $H_z \approx 0.22$, and the corresponding $d_{el} \approx 2.22 + 2/3 \approx 2.89$.

REFERENCES

Benzi, R., G. Paladin, G. Parisi, A. Vulpiani, 1984: J. Phys. A, 17, 3521.

Cahalan, R.F., 1990: Landsat Observations of Fractal Cloud Structure. (this volume).

Carter, P.H., R., Cawley, A. L. Licht, M.S. Melnik, 1986: Dimensions and entropies in chaotic systems. Ed. G. Mayer-Kress, p. 215-221, Springer.

Essex,C., 1990: Correlation dimension and data sample size. (this volume).

Frisch,U., G. Parisi, 1985: A multifractal model of intermittency, Turbulence and predictability in geophysical fluid dynamics and climate dynamics, 84-88, Eds. Ghil, Benzi, Parisi, North-Holland.

Davis, A., S. Lovejoy, and D. Schertzer 1990: Radiative transfer in multifractal clouds. (this volume).

Gabriel, P., S. Lovejoy, D. Schertzer, and G.L. Austin, 1988: Multifractal analysis of resolution dependence in satellite in satellite imagery, Geophys. Res. Lett., 15, 1373-1376.

Grassberger, P., 1983: Generalized dimensions of strange attractors. Phys. Lett., A 97, 227.

Halsey, T.C., M.H. Jensen, L.P. Kadanoff, I. Procaccia, B. Shraiman, 1986: Fractal measures and their singularities: the characterization of strange sets. Phys. Rev. A, 33, 1141-1151.

Hentschel, H.G.E., I. Proccacia, 1983: The infinite number of generalized dimensions of fractals and strange attractors, Physica, 8D, 435-444.

Lavallée, D., D. Schertzer, S. Lovejoy, 1990: On the determination of the codimension function. (this volume).

Lovejoy, S. 1981: Analysis of rain areas in terms of fractals, 20th conf. on radar meteorology, 476-484, AMS Boston.

Lovejoy, S., 1982: The area-perimeter relationship for rain and cloud areas. Science, 216, 185-187.

Lovejoy, S., B. Mandelbrot, 1985: Fractal properties of rain and a fractal model. Tellus, 37A, 209-232.

Lovejoy, S., D. Schertzer, 1985: Generalized scale invariance in the atmosphere and fractal models of rain. Wat. Resour. Res., 21, 1233-1250.

Lovejoy, S., D. Schertzer, 1986a: Scale invariance, symmetries fractals and stochastic simulation of atmospheric phenomena. Bull AMS 67, 21-32.

Lovejoy, S., D. Schertzer, A.A. Tsonis, 1987a: Functional box-counting and multiple elliptical dimensions in rain. Science, 235, 1036-1038.

Lovejoy, S., D. Schertzer, 1988: Extreme variability, scaling and fractals in remote sensing: analysis and simulation, Digital image processing in remote sensing, Ed. J. P. Muller, Francis and Taylor, 177-212.

---

[1] Unfortunately, the value of H estimated ($H=0.5\pm0.3$) is for the extreme large moments of the lidar returns, and in any case is not accurate enough to usefully estimate δ.

[2] Since δ depends on the various moments of the rain field considered, the generator G will in fact be stochastic, not constant as assumed for simplicity here (see Schertzer and Lovejoy, this volume).

Lovejoy, S., D. Schertzer, 1990a: Our multifractal atmosphere: a unique laboratory for nonlinear dynamics. Physics in Canada (in press).

Lovejoy, S., D. Schertzer, 1990b: Fractals, raindrops and resolution dependence of rain measurements, J. Appl. Meteor. (in press).

Lovejoy, S., D. Schertzer, 1990c: Multifractals, Universality Classes and Satellite and Radar Measurements of Cloud and Rain Fields, J. Geophy. Res., 95, 2021-2034.

Ludwig, F.L. K.C. Nitz, 1986: Analysis of lidar cross sections to determine the spatial structure of material in smoke plumes. Proc. of Smoke Obscurants Symposium, vol. 10, Harry Diamond Labs; Adelphis, Md., 231-241.

Mandelbrot, B., 1974: Intermittent turbulence in self-similar cascades: divergence of high moments and dimension of the carrier. J. Fluid Mech., 62, 331-350.

Mandelbrot, B., 1982: The Fractal Geometry of Nature. Freeman, 465pp.

Marshall, J.S., W.M. Palmer, 1948: The distribution of raindrops with size. J. Meteor., 5, 165-166.

Mauldin, R.D., S.C. Williams, 1986: Random recursive constructions: asymptotic geometric and topological properties. Trans. Am. Math. Soc., 295, 325-346.

Richardson, L.F., 1922: Weather prediction by numerical process, republished by Dover (1965).

Rhys, F.S., A. Waldvogel, 1986: Fractal shape of hail clouds. Phys. Rev. Lett. 56, 784-787.

Schertzer, D., S. Lovejoy, 1983: On the dimension of atmospheric motions. Preprint Vol., IUTAM Symp on Turbulence and Chaotic Phenomena in Fluids, 141-144.

Schertzer, D., S. Lovejoy, 1985a: The dimension and intermittency of atmospheric dynamics. Turbulent Shear Flow, 4, 7-33, Ed. B. Launder, Springer, NY.

Schertzer, D., S. Lovejoy, 1985b: Generalized scale invariance in turbulent phenomena. P.C.H. Journal, 6, 623-635.

Schertzer, D., S. Lovejoy, 1987a: Singularités anisotropes, et divergence de moments en cascades multiplicatifs. Annales Math. du Qué., 11, 139-181.

Schertzer, D., S. Lovejoy, 1987b: Physically based rain and cloud modeling by anisotropic, multiplicative turbulent cascades. J. Geophys. Res., 92, 9693-9714.

Schertzer, D., S. Lovejoy, 1988: Multifractal simulations and analysis of clouds by multiplicative processes. Atmospheric Research, 21, 337-361.

Schertzer, D., S. Lovejoy 1989: Generalized Scale invariance and multiplicative processes in the atmosphere. Pageoph, 130, 57-81.

Schertzer, D., S. Lovejoy, 1990a: Nonlinear geodynamical variability: multiple singularities, universality, observables. (this volume).

Schertzer, D., S. Lovejoy, 1990b: Nonlinear variability in geophysics: multifractal simulations and analysis, in Fractals: physical origins and properties, Ed. L. Pietronero, Plenum, New York, 49-79.

Schertzer, D., S. Lovejoy, R. Visvanathan, D. Lavallée, and J. Wilson, 1988: Universal Multifractals in Turbulence, in Fractal Aspects of Materials: Disordered Systems, Edited by D.A. Weitz, L.M. Sander, B.B. Mandelbrot, 267-269, Materials Research Society, Pittsburg, Pa.

Taylor, G. I., 1938: The spectrum of turbulence. Proc. Roy. Soc., A164, No. 919, 476-490.

Voss, R., 1983: Fourier Synthesis of Gaussian fractals: 1/f noises, landscapes and flakes. Proceedings, Siggraph Conf., Detroit, p1-21.

Welch, R.M., K.S. Kuo, B.A. Wielicki, S.K. Sengupta, L. Parker, 1988: Marine stratocumulus cloud fields off the coast of Southern California observed by LANDSAT imagery, part I: Structural characteristics. J. Appl. Meteor., 27, 341-362.

Wilson, J., D. Schertzer and S. Lovejoy, 1990: Physically based cloud modelling by scaling multiplicative cascade processes. (this volume).

Yano, J.-I., Takeuchi, Y., 1990: Fractal dimension analysis of horizontal cloud pattern in the intertropical convergence zone. (this volume).